

Atmospheric Stability Influences on Coupled Boundary Layer and Canopy Turbulence

EDWARD G. PATTON AND PETER P. SULLIVAN

National Center for Atmospheric Research, Boulder, Colorado*

ROGER H. SHAW

University of California, Davis, Davis, California

JOHN J. FINNIGAN

Commonwealth Scientific and Industrial Research Organisation, Canberra, Australian Capital Territory, Australia

JEFFREY C. WEIL

University of Colorado Boulder, Boulder, Colorado

(Manuscript received 6 March 2015, in final form 24 November 2015)

ABSTRACT

Large-eddy simulation of atmospheric boundary layers interacting with a coupled and resolved plant canopy reveals the influence of atmospheric stability variations from neutral to free convection on canopy turbulence. The design and implementation of a new multilevel canopy model is presented. Instantaneous fields from the simulations show that organized motions on the scale of the atmospheric boundary layer (ABL) depth bring high momentum down to canopy top, locally modulating the vertical shear of the horizontal wind. The evolution of these ABL-scale structures with increasing instability and their impact on vertical profiles of turbulence moments and integral length scales within and above the canopy are discussed. Linkages between atmospheric turbulence and biological control impact horizontal scalar source distributions. Decreasing spatial correlation between momentum and scalar fluxes with increasing instability results from ABL-scale structures spatially segregating momentum and scalar exchange at canopy top. In combination, these results suggest the need for roughness sublayer parameterizations to incorporate an additional length or time scale reflecting the influence of ABL-scale organized motions.

1. Introduction

Forests cover a significant fraction of Earth's land surface and provide a net land sink of carbon dioxide (CO_2) of over $10 \text{ GtCO}_2 \text{ yr}^{-1}$ (Le Quéré et al. 2014); of this $10 \text{ GtCO}_2 \text{ yr}^{-1}$, about one-third arises through carbon uptake from undisturbed tropical forests and two-thirds from undisturbed temperate and boreal forests. Regrowth on previously cleared tropical forest land and

in managed plantations contributes to an additional sink of $6.2 \text{ GtCO}_2 \text{ yr}^{-1}$, although this does not completely offset the even larger source ($\sim 10.25 \text{ GtCO}_2 \text{ yr}^{-1}$) resulting from ongoing clearing (Canadell and Schulze 2014). Even though deforestation is diminishing (FAO 2010), projections of the future global carbon balance are strongly influenced by our understanding of the response of the forest sink to climate change and disturbance. In addition to its involvement in the carbon cycle, forests play a critical role in Earth's climate through their influence on energy, water, and nitrogen cycles (Bonan 2008), as well as through exchanges of reactive species that place stringent controls on the atmosphere's oxidative capacity [or cleansing ability (e.g., Fuentes et al. 2000; Guenther et al. 2006)]. For all these reasons, understanding the processes controlling turbulent exchange of energy, momentum, and scalars between the

*The National Center for Atmospheric Research is sponsored by the National Science Foundation.

Corresponding author address: Edward G. Patton, National Center for Atmospheric Research, P. O. Box 3000, Boulder, CO 80307-3000.
E-mail: patton@ucar.edu

vegetation and the atmosphere has never been more important.

Vegetation (and urban) canopies produce turbulence that is qualitatively different to that over a rough surface, which ultimately results from canopies absorbing momentum over a distributed height range rather than at the ground surface. Within the canopy airspace, the distribution of the mean velocity and the turbulence is controlled by the interplay of downward turbulent transport of momentum and canopy drag (e.g., Raupach and Thom 1981) modulated by diabatic influences. The aerodynamic drag of the canopy varies spatially based upon the distribution of the canopy elements, their efficiency at extracting momentum, and the velocity field itself. Similarly, within-canopy distributions of scalars like heat, water vapor, and carbon dioxide are determined by the balance between turbulent transfer and the distribution of scalar sources and sinks. These, in turn, respond to solar radiation as it attenuates through the foliage, the biological state of the plants (e.g., their access to soil water), the ambient concentration of the particular scalar in the canopy airspace, and, in the case of reactive scalars, their reaction rates.

Current theory describing canopy exchange largely hinges on the hydrodynamic instability associated with an inflection point in the vertical profile of the horizontal wind at canopy top (sometimes called an inflection-point instability) induced through the canopy's distributed momentum absorption (e.g., Raupach et al. 1996; Finnigan et al. 2009). Parameterizations built upon this theory (Harman and Finnigan 2007, 2008) are showing great promise in predicting flux-gradient relationships (e.g., Weligepolage et al. 2012). However because the theory relies on the presence of wind speed shear at canopy top, its applicability across the broad stability variation that occurs outdoors remains uncertain. Consequently, this manuscript focuses on diabatically unstable conditions extending from high wind (near neutral) through increasingly weaker winds to no-wind situations (free convection).

Current understanding of the impact of atmospheric stability on canopy turbulence is based on a relatively limited number of studies (e.g., Leclerc et al. 1991; Su et al. 2004; Thomas and Foken 2007; Cava and Katul 2008; Dupont and Patton 2012a) where most of these are based upon measurements from a single tower and infer horizontal spatial variations in atmospheric properties by adopting Taylor's frozen turbulence hypothesis. Critically, these studies all lack information regarding atmospheric stability-induced variability of atmospheric boundary layer (ABL)-scale turbulence and its impact on turbulence at canopy scale.

Because of the vast range of scales present in the ABL, numerical simulation efforts attempting to further

the community's understanding of canopy turbulence have largely ignored ABL-scale turbulence and instead allocated numerical resolution toward resolving canopy processes as opposed to investigating larger domains (e.g., Shaw and Schumann 1992; Su et al. 1998; Dupont and Brunet 2008). For simplicity, these efforts have also targeted neutral stability conditions. Albertson et al. (2001) investigated atmospheric stability variations on coupled canopy turbulence but were similarly unable to interrogate the influence of ABL-scale turbulence because of domain size limitations. Bohrer et al. (2009) investigated stability variations in relatively large domains but with uncoupled canopy scalar sources/sinks.

To test the hypothesis that the evolution of organized turbulence structure across a range of atmospheric stability variations alters canopy exchange, this manuscript analyzes results from five large-eddy simulations (LES) of atmospheric boundary layers interacting with a resolved and interactive forest canopy. The manuscript is organized as follows: Section 2 describes the essentials of the LES code, and similarly, section 3 outlines the basis behind the multilevel canopy model. Section 4 sketches each model's configuration and the flow regimes investigated. Section 5 discusses how statistics are calculated and data normalization. Section 6 presents analysis of the results, and section 7 outlines the key findings regarding ABL control over canopy exchange that would not be possible with limited-domain numerical (or physical) simulations of canopy turbulence.

2. The large-eddy simulation

The National Center for Atmospheric Research's LES code has been described in a variety of earlier manuscripts (e.g., Moeng 1984; Moeng and Wyngaard 1988; Sullivan et al. 1996; Sullivan and Patton 2011). The current model is based on the developments described in Patton et al. (2005), Finnigan et al. (2009), and Sullivan and Patton (2011), where the equations for an atmospheric boundary layer under the Boussinesq approximation are solved on a discretized three-dimensional grid. The equations include: (i) transport equations for momentum $\mathbf{u} = (u, v, w)$ in the (streamwise x , spanwise y , and vertical z) directions, (ii) a transport equation for potential temperature θ , (iii) a transport equation for water vapor mixing ratio q , (iv) a discrete Poisson equation for pressure π to enforce incompressibility, and (v) an equation for subfilter-scale (SFS) turbulent kinetic energy e . Following Patton et al. (2005), buoyancy appears in the momentum equations as virtual potential temperature $\theta_v = \theta(1 + 0.61q)$.

Explicit spatial filtering (denoted by an overbar) of the equations in the presence of vegetative-canopy

elements generates terms representing canopy-induced processes (Raupach and Shaw 1982; Finnigan 1985; Finnigan and Shaw 2008); therefore, the equation set presented in Sullivan and Patton (2011) (with an additional equation for specific humidity) now appears as

$$\begin{aligned} \frac{\partial \bar{\mathbf{u}}}{\partial t} + \bar{\mathbf{u}} \cdot \nabla \bar{\mathbf{u}} &= -\nabla \cdot \mathbf{T} - f \hat{\mathbf{k}} \times (\bar{\mathbf{u}} - \mathbf{U}_g) \\ &\quad - \nabla \bar{\pi} + \hat{\mathbf{k}} \beta (\bar{\theta}_v - \theta_{v_0}) + F_d, \end{aligned} \quad (1)$$

$$\frac{\partial \bar{\theta}}{\partial t} + \bar{\mathbf{u}} \cdot \nabla \bar{\theta} = -\nabla \cdot \mathbf{B} + S_\theta, \quad (2)$$

$$\frac{\partial \bar{q}}{\partial t} + \bar{\mathbf{u}} \cdot \nabla \bar{q} = -\nabla \cdot \mathbf{Q} + S_q, \text{ and} \quad (3)$$

$$\frac{\partial \bar{e}}{\partial t} + \bar{\mathbf{u}} \cdot \nabla e = \mathcal{P} + \mathcal{B} + \mathcal{D} - \mathcal{E} - F_e, \quad (4)$$

where incompressibility is enforced by solving a discrete Poisson equation for pressure $\bar{\pi}$. In Eq. (1), f is the Coriolis parameter; $\hat{\mathbf{k}}$ is the unit vector in the vertical direction z ; \mathbf{U}_g is the geostrophic wind with horizontal (x, y) components (U_g, V_g); and $\beta = g/\theta_{v_0}$ is the buoyancy parameter, where g is Earth's gravitational acceleration and θ_{v_0} is a reference virtual potential temperature. The SFS momentum \mathbf{T} , heat \mathbf{B} , and moisture \mathbf{Q} fluxes and SFS energy e are:

$$\mathbf{T} = \bar{u}_i \bar{u}_j - \bar{u}_i \bar{u}_j, \quad (5)$$

$$\mathbf{B} = \bar{u}_i \bar{\theta} - \bar{u}_i \bar{\theta}, \quad (6)$$

$$\mathbf{Q} = \bar{u}_i \bar{q} - \bar{u}_i \bar{q}, \text{ and} \quad (7)$$

$$e = \frac{1}{2} (\bar{u}_i \bar{u}_i - \bar{u}_i \bar{u}_i). \quad (8)$$

In Eq. (4), \mathcal{P} and \mathcal{B} represent SFS shear and buoyancy production, respectively; \mathcal{D} represents SFS diffusion; and \mathcal{E} represents dissipation. These terms are modeled using the turbulent eddy viscosity ν_t and diffusivity ν_H approach described in Deardorff (1980).¹

In Eqs. (1)–(4), F_d , S_θ , S_q , and F_e represent the canopy-induced contributions that appear as a result of spatially filtering the flow equations in the multiply connected canopy airspace that surrounds the canopy elements; hence, above the canopy these terms are zero. Within the canopy, F_d combines the canopy's pressure and viscous drag forces, where viscous drag is assumed to be negligible compared to pressure drag (Thom 1968)

¹ Note that Sullivan et al.'s (1994) two-part SFS model—which presumes that the primary momentum sink becomes increasingly underresolved with approach to the surface—is not applicable for the situation studied here where the primary momentum sink (i.e., the canopy) is resolved.

and is parameterized following Shaw and Schumann (1992) as

$$F_d = -c_d a |\bar{\mathbf{u}}| \bar{\mathbf{u}}, \quad (9)$$

where a is a one-sided frontal plant area density (PAD), c_d is a dimensionless drag coefficient describing the efficiency of that PAD at extracting momentum, and $|\bar{\mathbf{u}}|$ is the instantaneous wind speed. Following Shaw and Patton (2003), wakes shed in the lee of canopy elements are presumed small enough that they directly dissipate to heat. Therefore, F_e solely represents the work performed by SFS motions against canopy drag, which is parameterized as

$$F_e = -\frac{8}{3} c_d a |\bar{\mathbf{u}}| e \quad (10)$$

under the assumption that SFS turbulence is isotropic. In Eqs. (2) and (3), S_θ and S_q describe the canopy-induced heat or moisture sources from the canopy, which also appear through spatially filtering the atmospheric scalar conservation equations in the presence of the solid canopy elements. The sources S_θ and S_q are parameterized using a multilevel coupled land surface model implemented at every horizontal grid point within the LES. This canopy-resolving land surface model will be described more fully in section 3.

Boundary conditions are periodic in the horizontal, and the upper-boundary condition is such that horizontal velocities, SFS energy, potential temperature, and specific humidity use a specified gradient method (Neumann conditions) and vertical velocity is forced to 0 m s^{-1} (Dirichlet condition). Beneath the canopy, rough-wall boundary conditions (i.e., specified roughness length z_*) are imposed based upon a drag rule for which the transfer coefficients are determined via Monin–Obukhov similarity theory (Moeng 1984), which is a reasonable assumption since the resolved canopy serves as the dominant sink for momentum and acts as the primary heat/moisture source.² Spalart et al.'s (1991) third-order Runge–Kutta scheme advances the solutions in time. Horizontal spatial derivatives use Orszag's (1969) pseudospectral methods for all field variables, while vertical derivatives use second-order finite differences

² We note that we apply a Monin–Obukhov boundary condition because the community lacks a better option. To accommodate free convection, we follow Schmidt and Schumann (1989) by applying Monin–Obukhov similarity theory locally at every grid point and enforcing a small minimum near-surface convective velocity of $0.07(g C_H \Delta \theta_v / \theta_{v_0})^{1/3}$, where C_H is a locally derived surface exchange coefficient according to Monin–Obukhov similarity theory.

for momentum and SFS energy and Beets and Koren's (1996) monotone scheme for potential temperature and specific humidity.

3. The land surface model

a. The model's basis

The NOAA/NCEP–Oregon State University–Air Force Research Laboratory–NOAA/Office of Hydrology land surface model (Noah) serves as the primary basis describing the coupling between the atmosphere and the land surface. Noah is designed for weather forecasting focusing on hydrologic coupling in the soil–water–vegetation system (Chen et al. 1996; Chen and Dudhia 2001; Ek et al. 2003). In its standard form (e.g., Ek et al. 2003), Noah's canopy exchanges heat and moisture as a single “big leaf” and assumes that emitted scalars are vented immediately from the canopy space (e.g., Pan and Mahrt 1987). Sensible and latent heat fluxes are determined through a coupling between radiation and photosynthesis models to obtain a surface resistance and the solution of the energy balance using Monteith's (1973) resistance method. In the soil, Noah predicts vertical profiles of temperature and moisture using a one-dimensional model with specified lower-boundary conditions [see Ek et al. (2003) for further details]. Noah was previously coupled with NCAR's LES code to investigate the effects of a horizontally varying soil moisture content on the mean and turbulence structure of the ABL (Patton et al. 2005); therefore, the interface between the two codes is already well established.

b. The multilayer canopy

In the current implementation, Noah's big-leaf model has been extended so that the canopy now spans multiple vertical levels. Noah remains a 1D column model implemented at every horizontal location, but the canopy extends vertically into the flow domain according to the prescribed PAD described in section 2. Leaf energy balances are now solved at each vertical level, resolving the canopy based upon the vertical distribution of radiant energy and LES-derived local atmospheric temperature, moisture and wind. The new vertically resolved canopy model arises through merging a number of previously developed models into Noah's simpler canopy system.

New to Noah is a canopy radiation model that stems from Guenther et al.'s (1995, 2006) Model of Emissions of Gases and Aerosols from Nature (MEGAN). Incoming solar radiation is imposed as an external forcing. Sunlit leaves experience incoming direct longwave radiation according to local air temperature modified on the sunlit side to account for Brutsaert's (1975) apparent

clear-sky emissivity, while direct incoming longwave radiation for shaded leaves is calculated based solely upon local air temperature. MEGAN uses specified leaf scattering, reflection, and clumping coefficients for visible and near-infrared (NIR) wavelength radiation (Table 2). Using these coefficients in combination with an assumed spherical leaf angle distribution, the vertically varying absorption and scattering of direct/diffuse visible and NIR radiation by both sunlit and shaded leaves (Goudriaan and van Laar 1994; Leuning et al. 1995; Leuning 1997) is determined.

Stomatal resistance r_s is calculated using a photosynthesis-based formulation following the gas exchange evapotranspiration model (GEM) (Niyogi et al. 2009), which at the time collected the latest leaf-level photosynthesis–carbon assimilation–transpiration understanding (Collatz et al. 1991, 1992; Leuning 1990; Leuning et al. 1995) into a single framework. Applying the biophysical components of GEM at the meter scale should be reasonable since the functions determining these components were largely derived from leaf-level measurements (Bonan 1996); however, for the implementation presented here, the exchange is scaled by each grid volume's PAD a . Currently, the atmospheric CO₂ partial pressure is assumed constant at 34 Pa.

Solving the leaf energy balance for leaf temperature $\bar{\theta}_l$ follows Nikolov et al.'s (1995) quartic form and uses a bisection method to iterate for the solution. Estimating the leaf boundary layer resistance for heat r_b follows Leuning et al. (1995), but Niyogi et al.'s (2009) strategy to use the maximum of Leuning et al.'s (1995) forced- or free-convective forms is adopted. Leaf temperature then defines the within-leaf saturation water vapor density [i.e., $\bar{q}_l = q_{\text{sat}}(\bar{\theta}_l)$]. Spatially varying heat and moisture sources from the vegetation to each atmospheric grid volume [i.e., S_θ and S_q in Eqs. (2) and (3), respectively] are then calculated based on the local heat/moisture gradient between the leaves and the atmosphere and the appropriate combination of leaf boundary layer and stomatal resistance: that is,

$$S_\theta = 2 \frac{\bar{\theta}_l - \bar{\theta}}{r_b} a \quad \text{and} \quad (11)$$

$$S_q = \frac{\bar{q}_l - \bar{q}}{1.075^{-1} r_b + r_s} a, \quad (12)$$

where the factor of 2 in Eq. (11) arises because heat exchange occurs on both sides of the leaves, and the 1.075^{-1} factor in Eq. (12) follows from Leuning et al. (1995); the latter factor arises because of a different effective boundary layer thickness for mass versus heat under forced convection (Monteith and Unsworth 2008). The variables $\bar{\theta}$ and \bar{q} are the atmospheric temperature

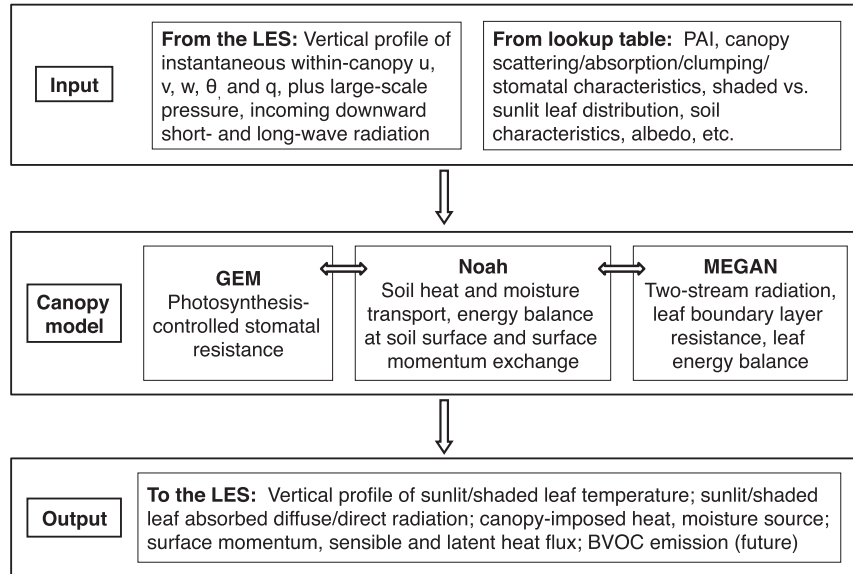


FIG. 1. Schematic outlining the coupling between a 1D profile of external data from the LES driving the multilevel canopy model and the quantities output from the multilevel canopy model driving the LES code. Currently only the canopy-induced heat and moisture sources and the surface momentum and sensible and latent heat fluxes are felt by the LES.

and water vapor specific humidity values from the within-canopy solutions to Eqs. (2) and (3) converted to the appropriate units. Figure 1 provides a flowchart describing the coupling between the LES and the multilevel canopy model; the appendix presents an evaluation of the model against observations from the Canopy Horizontal Array Turbulence Study (CHATS; Patton et al. 2011).

4. Simulation design

a. The atmosphere

The simulations use (2048, 2048, 1024) grid points in a Cartesian coordinate system resolving a (5120, 5120, 2048)-m domain using (2.5, 2.5, 2)-m resolution in the (x , y , z) directions, respectively. The horizontal domain size is chosen to span a distance approximately 5 times the anticipated ABL depth ($z_i \sim 1$ km), thereby minimizing the influence of the horizontal periodic boundary conditions and positioning the upper boundary sufficiently far from the entrainment zone. The chosen resolution amply satisfies Sullivan and Patton's (2011) requirements for resolution-independent solutions, while permitting the flow to feel the presence of the resolved and interactive canopy.

The simulation's location is 38°N, 121°W, representative of Dixon, California [the location of the CHATS field campaign (Patton et al. 2011)]. The simulations begin at 1100 LT, with an imposed solar constant of 1367 W m^{-2} and an atmospheric transmissivity according

to Stull (1988), where the transmissivity without clouds varies between 0.6 when the sun is at the horizon and 0.8 when the sun is at the solar zenith. Therefore, the incoming solar radiation impinging at the top of the trees starts at about 940 W m^{-2} at 1100 LT and evolves to approximately 1015 W m^{-2} throughout the simulation.

The primary parameter variation across the simulations involves the imposed geostrophic wind (U_g , V_g), where U_g (in the streamwise direction) varies between 20 and 0 m s^{-1} , resulting in atmospheric stability variations ranging from near-neutral to free-convective conditions (i.e., $1 > -z_i/L > \infty$). See Table 1 for further details.

The initial conditions impose the following: 1) a constant mean horizontal wind (u , v) everywhere in the domain equal to (U_g , V_g); 2) a constant potential temperature θ profile of 300 K from the surface to a height of 40 m (twice the canopy height) and then linearly increasing with height at a constant rate of 3 K km^{-1} above that height; 3) a constant water vapor specific humidity q profile of 1 g kg^{-1} ; and 4) a constant SFS energy e profile of $1 \times 10^{-8} \text{ m}^2 \text{s}^{-2}$. Divergence-free perturbations placed on the horizontal velocity fields across the five vertical grid points centered at canopy top with an amplitude of 0.001 m s^{-1} and an increased SFS energy to $1 \text{ m}^2 \text{s}^{-2}$ over the same vertical extent initiate the turbulence.

b. The canopy-resolving land surface model

The vegetation is horizontally homogeneous, 20 m tall ($h = 20 \text{ m}$), and vertically resolved by 10 grid points

TABLE 1. Parameters characterizing the simulated atmosphere for each simulation. (U_g, V_g) represents the imposed geostrophic wind in the (x, y) directions; $u_* = (\langle u'w' \rangle^2 + \langle v'w' \rangle^2)^{1/4}$ is the friction velocity; $\langle w'\theta'_v \rangle$ is the buoyancy flux; $B = H/LE$ is the Bowen ratio ($H = \rho c_p \langle w'\theta' \rangle$ is the sensible heat flux and $LE = \rho L_v \langle w'q' \rangle$ is the latent heat flux); z_i is the ABL depth; $L = -(u_*^3 \theta_{v*}) / (\kappa g c_p \langle w'\theta'_v \rangle)$ is the Obukhov length; $\delta_\omega = 2\langle u_h \rangle / [\partial \langle u_h \rangle / \partial z]$ is the vorticity thickness; $w_* = (g \langle w'\theta'_v \rangle z_i / \theta_{v*})^{1/3}$ is the Deardorff convective velocity scale; and $w_m = (w_*^3 + 5u_*^3)^{1/3}$ is a scaling velocity combining both shear and buoyancy forcing. The parameters u_* , $\langle w'\theta'_v \rangle$, B , L , δ_ω , w_* , and w_m are horizontally and time-averaged quantities evaluated at canopy top. Parameters θ_* and q_* are potential temperature and specific humidity scales defined as the total scalar source into the domain divided by w_m ; that is, $\theta_* = (\int_0^h \langle S_\theta \rangle dz + \langle w'\theta' \rangle_0) \times w_m^{-1}$, and $q_* = (\int_0^h \langle S_q \rangle dz + \langle w'q' \rangle_0) \times w_m^{-1}$, where $\langle w'\theta' \rangle_0$ and $\langle w'q' \rangle_0$ are the fluxes of potential temperature and specific humidity at the underlying soil surface, respectively.

Name	(U_g, V_g) (m s $^{-1}$)	u_* (m s $^{-1}$)	$\langle w'\theta'_v \rangle$ (m K s $^{-1}$)	B	z_i (m)	L (m)	$-z_i/L$	δ_ω (m)	w_* (m s $^{-1}$)	w_m (m s $^{-1}$)	θ_* (K)	q_* (kg kg $^{-1}$)
NN	(20, 0)	1.37	0.24	5.4	742	-827	0.9	24.5	1.82	2.67	0.09	6.6×10^{-6}
WU	(10, 0)	0.86	0.21	2.6	995	-233	4.3	25.6	1.89	2.15	0.10	1.5×10^{-5}
MU	(5, 0)	0.56	0.20	3.3	952	-69	13.8	27.6	1.84	1.93	0.10	1.6×10^{-5}
SU	(2, 0)	0.34	0.20	3.0	958	-14	67.2	29.2	1.86	1.87	0.10	1.6×10^{-5}
FC	(0, 0)	0.07	0.23	4.7	1207	0	∞	34.8	2.07	2.07	0.11	9.1×10^{-6}

with a PAD profile a representative of a deciduous canopy with a relatively dense overstory and a relatively open trunk space (Fig. 2); vertical integration of the plant area density profile yields a one-sided plant area index (PAI) of 2. Following MEGAN (Guenther et al. 1995, 2006), the plant functional type (PFT) imposes characteristics similar to a generic broadleaf deciduous forest; the specifics for this PFT can be found in Table 2. The leaf area fraction considered sunlit or shaded is prescribed at each level according to an exponential function of cumulative leaf area downward from canopy top modulated by the PFT's clustering coefficient (Fig. 2 and Table 2).

The soil is resolved using four vertical levels centered at depths of (0.05, 0.20, 0.45, 0.80) m, with a specified lower temperature boundary condition of 295 K at 1 m. The soil characteristics mimic silty-clay loam, with hydraulic and thermal properties taken directly from Noah (Table 3; Chen et al. 1996; Chen and Dudhia 2001; Ek et al. 2003). The soil's surface roughness z_* is 0.001 m with an albedo of 0.2. Initial soil conditions come from a 2-yr High-Resolution Land Data Assimilation System (HRLDAS; Chen et al. 2007) simulation developed for simulating the CHATS data (Patton et al. 2011); Table 4 presents the initial soil moisture and temperature profiles.

c. Computational aspects

The simulations required between 100 and 225 wall-clock hours running on 16384 computer cores, totaling between 1.5 and 3.7×10^{-6} CPU hours per simulation. As described in Sullivan and Patton (2011), to accommodate pseudospectral differencing, the NCAR LES code uses the Message Passing Interface (MPI) to partition the computational domain into

horizontal “bricks” or “pencils.” Because the vegetative canopy resides at the lowermost portion of the domain, the bricks are transposed vertically, allowing every processor to participate in solving the required energy balances determining the next time step's scalar source distribution throughout the canopy and the underlying surface fluxes at each horizontal grid point. To allow checkpointing during the simulation, the code uses MPI input/output to read/write data volumes; a single instant in time for these simulations requires approximately 245 GB of storage.

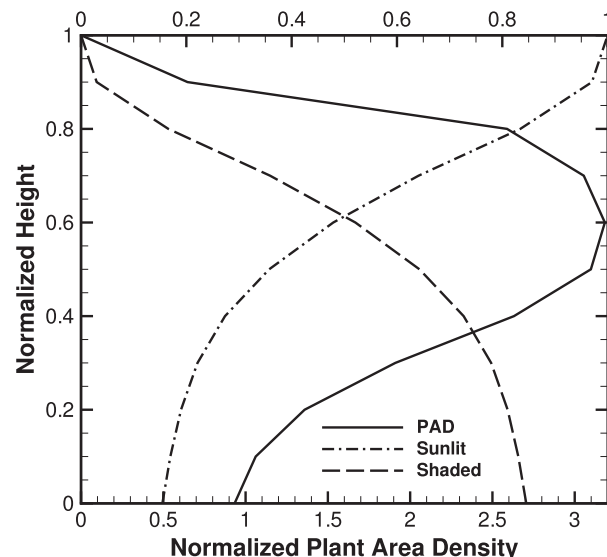


FIG. 2. Vertical profiles relative to the height of the canopy h of horizontally homogeneous one-sided plant area density ($m^2 m^{-3}$; solid) normalized by the canopy height (lower axis), the fraction of the one-sided plant area density that is sunlit (upper axis; dashed-dotted), and the fraction of the one-sided plant area density that is shaded (upper axis; long dashed).

TABLE 2. Parameters specified for the broadleaf deciduous canopy [from MEGAN (Guenther et al. 2006)]. Radiation is given as photosynthetically active radiation (PAR) and near-infrared (NIR).

Parameter	Value/type
Leaf width	0.05 m
Leaf length	0.15 m
Scattering coefficient PAR	0.2
Scattering coefficient NIR	0.8
Reflection coefficient PAR	0.057
Reflection coefficient NIR	0.389
Clumping coefficient	0.85
Leaf emissivity	0.95
Transpiration type	Hypostomatous

5. Averaging and scaling

During the simulations, turbulent fluctuations are calculated at every time step as deviations from instantaneous horizontally averaged fields. Higher-order moments are then created by horizontally averaging fluctuation products. Using these time-varying horizontally averaged profiles, the boundary layer-averaged turbulent kinetic energy (TKE) is interrogated to determine whether the flow has reached quasi equilibrium with the forcing; that is, the TKE averaged over the depth of the ABL has become steady in time. Time averaging then commences, and profiles are averaged over the subsequent 3600 s (1 h) of simulated time. In what follows, angle brackets denote this time- and horizontal-averaging process, and a prime represents the fluctuations. For clarity, the overbar notation introduced in section 2 denoting the explicit filtering process will be dropped, and all turbulent moments presented will include the sum of resolved and subfilter-scale contributions.

To compare the simulations, results are presented in normalized form. Two characteristic length scales are used: 1) the ABL depth z_i , which is calculated using the maximum gradient method (Sullivan et al. 1998; Davis et al. 2000) and will occasionally be referred to as “ABL scale,” and 2) the canopy height h . Since the flows in each simulation respond to the varying combinations of shear and buoyancy forcing, we use a velocity scale w_m incorporating both influences (Moeng and Sullivan 1994); w_m is calculated using canopy-top values of the vertical buoyancy flux $\langle w'\theta'_v \rangle$ and friction velocity u_* as follows:

$$w_m = (w_*^3 + 5u_*^3)^{1/3}, \quad (13)$$

where $w_* = (g\langle w'\theta'_v \rangle z_i / \theta_{v*})^{1/3}$ is the Deardorff convective velocity scale, $u_* = (\langle u'w' \rangle^2 + \langle v'w' \rangle^2)^{1/4}$. The factor

TABLE 3. Parameters characterizing the silty-clay-loam soil, Noah's soil class number 8.

Parameter	Value/type
b exponent	8.72
Threshold at which direct soil evaporation ends	$0.120 \text{ m}^3 \text{ m}^{-3}$
Threshold at which soil saturates	$0.464 \text{ m}^3 \text{ m}^{-3}$
Reference soil moisture (field capacity)	$0.387 \text{ m}^3 \text{ m}^{-3}$
Wilting point (soil moisture)	$0.120 \text{ m}^3 \text{ m}^{-3}$
Saturation soil matric potential	0.617 m
Saturated hydraulic conductivity	$2.04 \times 10^{-6} \text{ m s}^{-1}$
Saturated soil water diffusivity	$2.37 \times 10^{-3} \text{ m}^2 \text{ s}^{-1}$
Soil heat capacity	$2.60 \times 10^6 \text{ J m}^{-3} \text{ K}^{-1}$
Quartz fraction	0.10

5 arises in the scaling by presuming that the entrainment buoyancy flux is a factor of 0.2 times the surface buoyancy flux; it has also been assumed that Moeng and Sullivan's (1994) A parameter is 1.

Scalar fields are normalized by their respective total source strength divided by w_m :

$$\theta_* = \left(\int_0^h \langle S_\theta \rangle dz + \langle w'\theta' \rangle_0 \right) \times w_m^{-1} \quad \text{and} \quad (14)$$

$$q_* = \left(\int_0^h \langle S_q \rangle dz + \langle w'q' \rangle_0 \right) \times w_m^{-1}. \quad (15)$$

In the parentheses in Eqs. (14) and (15), the left-hand portion denotes the vertically integrated horizontally and time-averaged canopy-source distribution, and the right-hand portion denotes the respective scalar flux at the underlying soil surface. Table 1 presents values of these scaling parameters for each simulation.

6. Results and discussion

a. Velocity

1) HORIZONTAL SLICES

Horizontal slices of instantaneous streamwise and vertical velocity at $z/h = 6$ from four simulations (Figs. 3 and 4, respectively) reveal the variation of the ABL-scale motions with atmospheric stability. In shear-dominated weakly unstable conditions (WU; Figs. 3a, 4a), velocity fields tend to organize themselves into

TABLE 4. The initial volumetric soil moisture content and soil temperature profiles.

Depth (m)	Moisture ($\text{m}^3 \text{ m}^{-3}$)	Temperature (K)
0.05	0.222	292.4
0.20	0.236	291.3
0.45	0.236	290.1
0.80	0.236	289.0

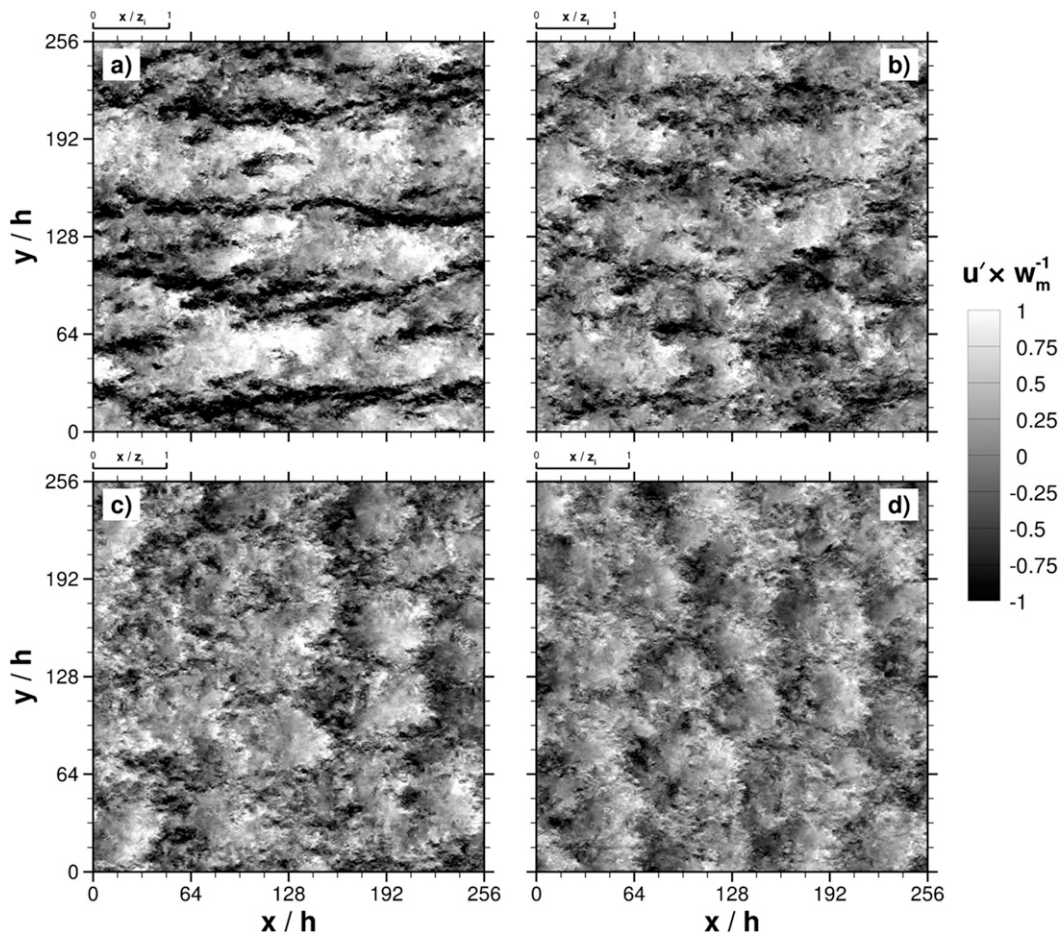


FIG. 3. Horizontal slices of instantaneous streamwise velocity fluctuations relative to the horizontal mean normalized by w_m from four simulations, where $-z_i/L$ = (a) 4.3 (WU), (b) 13.8 (MU), (c) 67.2 (SU), and (d) ∞ (FC). The slices are taken from a height of 120 m or $z/h = 6$. The short axis above each panel depicts the ABL depth z_i for each simulation.

elongated roll-like structures aligned with the geostrophic wind, while in free convection (FC; Figs. 3d, 4d), the velocity fields organize in cellular patterns. Intermediate stabilities (Figs. 3b,c, 4b,c) reveal a progression between these two end-member states.

This evolution of ABL-scale motions with stability has been well established over the years (e.g., Deardorff 1972; Moeng and Sullivan 1994; Khanna and Brasseur 1998). Using linear-stability analysis, H. Jonker et al. (2015, unpublished manuscript) shows that this variation results from a competing balance between shear- and buoyancy-generated instabilities leading to preferential growth of particular longitudinal or transverse modes.

Features to note in Figs. 3 and 4 include the following: first, the structures to scale approximately with the ABL depth z_i (Table 1); and, second, the skewed vertical velocity field distribution in the horizontal (i.e., relatively strong rising motions occurring in narrowly

confined bands, with relatively weaker sinking motions occurring over broader regions).

The elongated roll structures in WU [and near neutral (NN); not shown] and the transition to cellular structure [in moderately unstable (MU) \rightarrow FC] remain observable in the canopy-top streamwise velocity fields (Fig. 5), reminiscent of the results of Hutchins and Marusic (2007) who found the signature of very large structures in their observations collected within a neutrally stratified log layer. Across all stabilities, the ABL-scale organized motions generate broad regions of negative vertical velocity, bringing high-streamwise-momentum fluid to canopy top with a visible smaller-scale structure embedded within. The signature of ABL-scale motions is less evident in instantaneous canopy-top vertical velocity (Fig. 6), as vertical motions are strongly impacted by proximity to the canopy and to the underlying soil surface. Compared to the vertical velocity's cellular-like

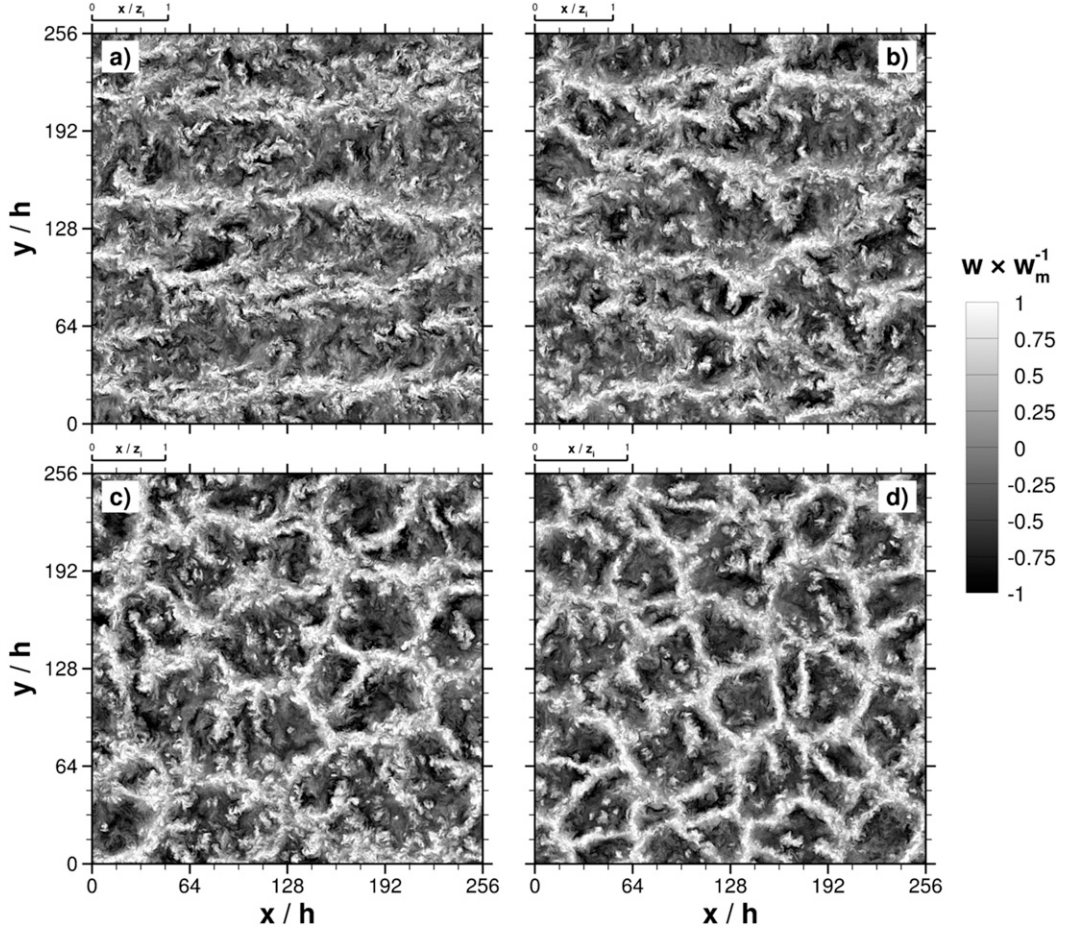


FIG. 4. Horizontal slices of instantaneous vertical velocity normalized by w_m from four simulations, where $-z_i/L =$ (a) 4.3 (WU), (b) 13.8 (MU), (c) 67.2 (SU), and (d) ∞ (FC). The slices are taken from a height of 120 m or $z/h = 6$. The short axis above each panel depicts the ABL depth z_i for each simulation.

structure that was evident at $z/h = 6$, the smaller scales contained within the canopy-top vertical velocity fields appear more filament-like with increasing instability (NN \rightarrow FC).

Based on observed streamwise velocity profiles averaged over short times (10 s), Gao et al. (1992) found that canopy-scale organized motions were preceded by profiles exhibiting strong streamwise velocity shear at canopy top; Shaw et al. (1990) suggested that favorable pressure gradients were likely responsible. The simulations discussed here demonstrate that the spatial distribution, magnitude, and duration of canopy-top streamwise velocity are strongly controlled by organized ABL-scale motions that modulate the local vertical shear.

2) STATISTICS

The NCAR LES code's ability to reproduce statistics of ABL flows across a range of stability conditions has been previously documented in the literature and

compared against observations (e.g., Moeng and Sullivan 1994; Beare et al. 2006; Sullivan and Patton 2011; Lenschow et al. 2012). With the exception of Dwyer et al. (1997) and Patton et al. (2003), most studies of canopy flows using NCAR's LES code have focused on neutral stability conditions (Patton 1997; Su et al. 2000; Shaw and Patton 2003; Finnigan et al. 2009). Dwyer et al. (1997) presented a study of buoyancy influences on turbulent kinetic energy budgets, but the simulations were carried out in small domains that were unable to capture the large scales of motion described in the previous section. Patton et al. (2003) overcame the limited-domain issue using nested grids to investigate the influence of a canopy on ABL flow and scalar statistics; statistics investigated in that study compared well with measurements but focused on a single atmospheric stability with an imposed canopy-source distribution. For these numerous reasons, the following discussion therefore refrains from presenting atmospheric stability

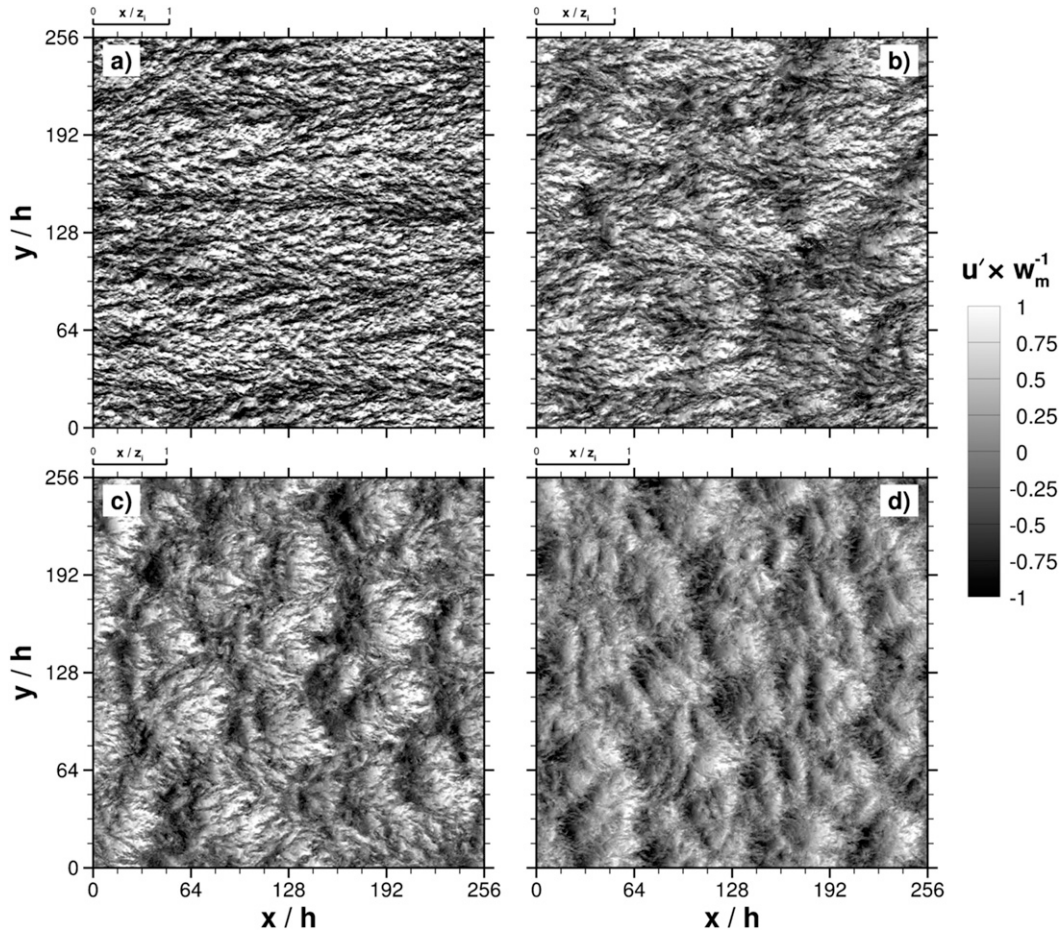


FIG. 5. Horizontal slices of instantaneous streamwise velocity fluctuations relative to the horizontal mean normalized by w_m from four simulations, where $-z_i/L$ = (a) 4.3 (WU), (b) 13.8 (MU), (c) 67.2 (SU), and (d) ∞ (FC). The slices are taken from a height of 20 m or $z/h = 1$. The short axis above each panel depicts the ABL depth z_i for each simulation.

impacts on the overall ABL flow statistics and instead focuses on stability's impact on statistics of canopy turbulence.

Vertical profiles from the ground up to $z/h = 4$ [or $z/z_i = (0.11 \rightarrow 0.07)$ for (NN \rightarrow FC)] of normalized wind speed (Fig. 7a) reveal the primary result of varying U_g from 20 to 0 m s^{-1} . Horizontal wind speeds [$\langle u_h \rangle = (\langle u \rangle^2 + \langle v \rangle^2)^{1/2}$] at canopy top vary from $(1.69, 1.26, 0.85, 0.38, 0.00) \times w_m$ for cases [NN, WU, MU, strongly unstable (SU), FC], respectively. Coincident with this wind speed reduction at canopy top, the mean wind speed's vertical gradient at canopy top varies from $(1.93, 1.39, 0.79, 0.36, 0.01) \times w_m^{-1}h$. Both the horizontal wind and the vertical shear of the horizontal wind decrease with increasing instability; however, vertical shear decreases more quickly than does the mean wind speed. Therefore, the vorticity thickness at canopy top [$\delta_\omega = 2\langle u_h \rangle / (\partial \langle u_h \rangle / \partial z)$] increases with increasing instability

(Table 1). Figure 7a reveals no subcanopy wind speed maximum across all five simulations. The lack of subcanopy wind speed maximum results from a smaller-magnitude vertical divergence of within-canopy turbulent momentum flux transport compared to the magnitude of the pressure–velocity gradient covariance for all cases (not shown), consistent with Shaw (1977).

Normalized standard deviations of velocity (Figs. 7b–d) decrease in a natural progression in response to increasing instability; $(\sigma_u \text{ and } \sigma_v) \times w_m^{-1}$ are mostly constant above the canopy, with canopy-top magnitudes of $\sim(0.97, 0.72)$ for NN and $(0.43, 0.42)$ for FC, respectively. Both σ_u and σ_v reveal a slight above-canopy maximum, with σ_u peaking at elevations somewhat higher above the canopy ($z/h \sim 2.5$) than σ_v ($z/h \sim 1.5$). Consistent with field measurements (e.g., Dupont and Patton 2012a), σ_u and σ_v rapidly diminish with descent into the canopy, a feature arising from diminishing shear

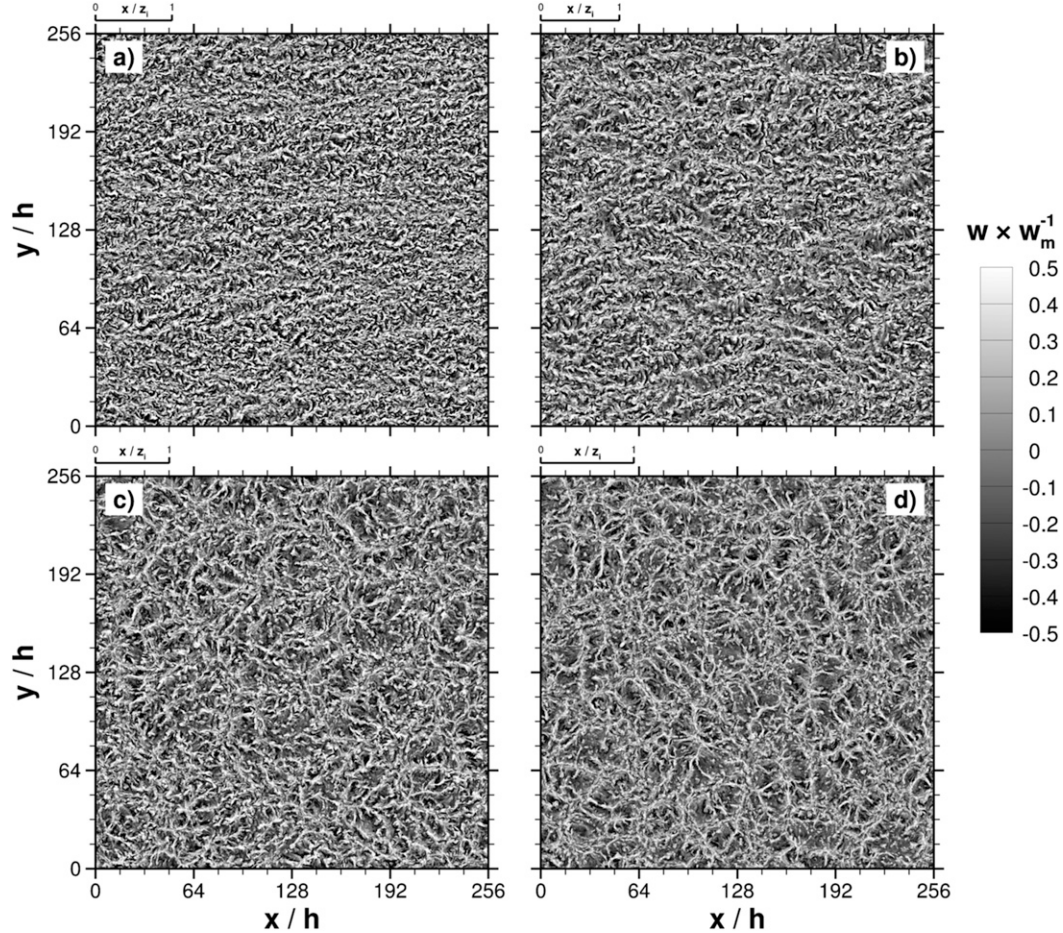


FIG. 6. Horizontal slices of instantaneous vertical velocity normalized by w_m from four simulations, where $-z_i/L =$ (a) 4.3 (WU), (b) 13.8 (MU), (c) 67.2 (SU), and (d) ∞ (FC). The slices are taken from a height of 20 m or $z/h = 1$. The short axis above each panel depicts the ABL depth z_i for each simulation.

production of σ_u in response to work performed against canopy drag and subsequently reduced redistribution of σ_u through pressure strain resulting in reduced σ_v production. Interestingly, σ_v increases again in the relatively open trunk space for all cases, while σ_u only reveals a similar increase under weaker wind conditions.

For near-neutral conditions (WU, NN), $\sigma_w \times w_m^{-1}$ is almost constant with height above the canopy, but with increasing instability, $\sigma_w \times w_m^{-1}$ 1) diminishes at canopy top and 2) increases with height above the canopy as buoyantly driven plumes become the primary turbulence-generating mechanism; this second feature is also seen in recent field data (e.g., Dupont and Patton 2012a). Consistent with Katul et al.'s (1998a) observations, the above-canopy variation of $\sigma_w \times w_m^{-1}$ for FC follows the shape of Wyngaard et al.'s (1971) free-convection prediction [i.e., $\sigma_w/w_* = 1.34 \times (z/z_i)^{1/3}$, which can be re-written for this case in terms of canopy height as $\sigma_w/w_* \approx 0.34 \times (z/h)^{1/3}$], but the LES results are about

20% smaller than Wyngaard et al.'s (1971) prediction (not shown). Below canopy top, $\sigma_w \times w_m^{-1}$ diminishes almost linearly with height for all cases as distance from the underlying surface dominates the vertical velocity spectrum [a feature that will be further discussed in section 6a(3)]. The SFS contribution to the total turbulent kinetic energy is small, ranging from 9% (NN) to 6% (FC) and occurring at the lowest model level in all cases except NN, where it occurs at $z/h = 0.5$.

For comparison with the velocity standard deviations, it is useful to define a height-dependent measure of the vertical turbulent flux of horizontal momentum with the dimensions of velocity [e.g., $\langle u_{*a} \rangle = (\langle u'w' \rangle^2 + \langle v'w' \rangle^2)^{1/4}$]. Because z_i ranges from 800 to 1200 m (or from 40 to 60 canopy heights) in these simulations (Table 1), profiles of $\langle u_{*a} \rangle \times w_m^{-1}$ appear nearly constant with height above the canopy (Fig. 7e), consistent with tower-based observations (e.g., Dupont and Patton 2012a). Canopy-top values of $\langle u_{*a} \rangle \times w_m^{-1}$ diminish with increasing instability

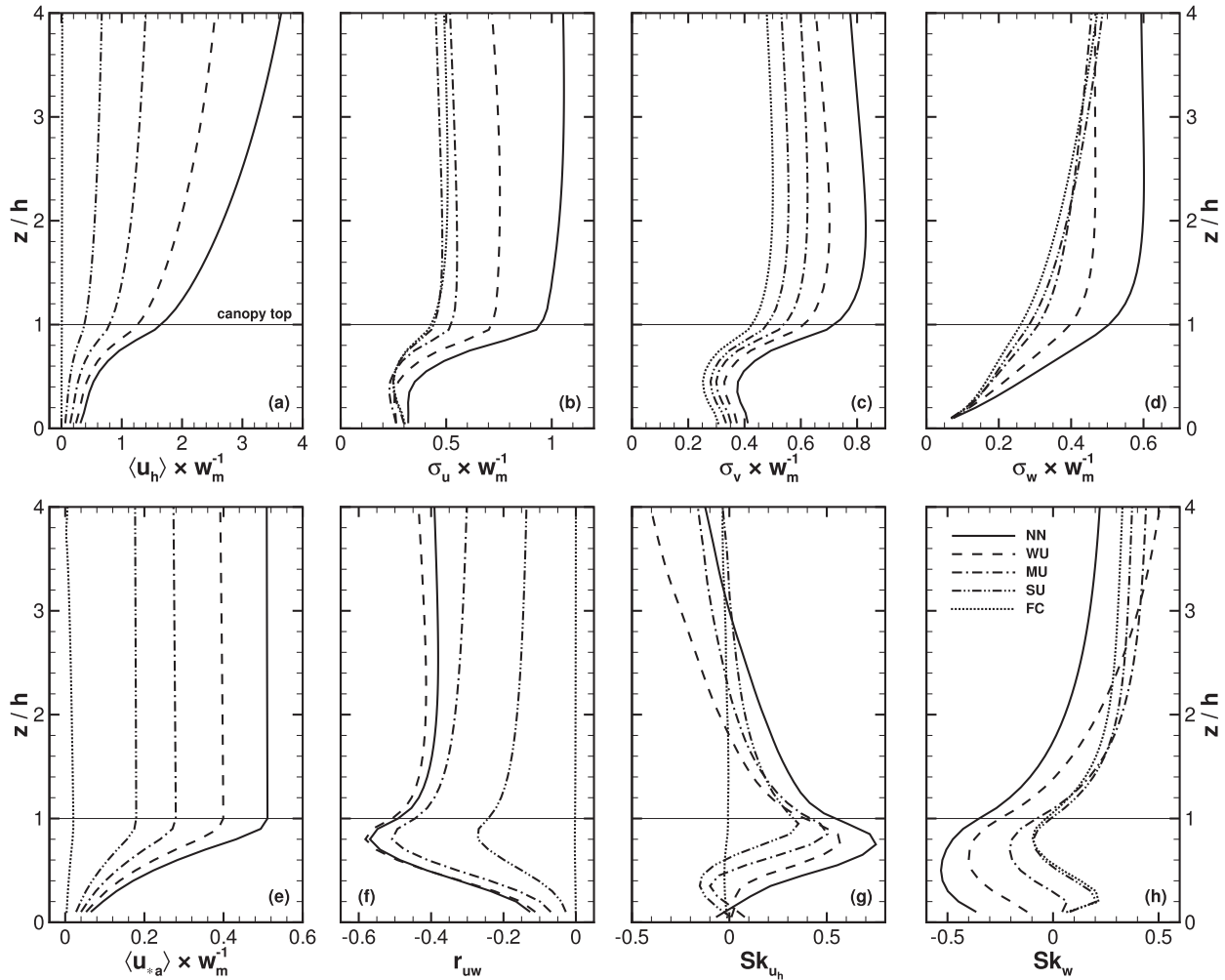


FIG. 7. Horizontal- and time-averaged vertical profiles of (a) normalized horizontal wind speed [$\langle u_h \rangle = (\langle u \rangle^2 + \langle v \rangle^2)^{1/2}$], (b) normalized standard deviation of the streamwise velocity ($\sigma_u = \langle u'^2 \rangle^{1/2}$), (c) normalized standard deviation of the spanwise velocity ($\sigma_v = \langle v'^2 \rangle^{1/2}$), (d) normalized standard deviation of the vertical velocity ($\sigma_w = \langle w'^2 \rangle^{1/2}$), (e) normalized square root of the vertical flux of horizontal momentum [$\langle u_{*a} \rangle = ((\langle u'w' \rangle^2 + \langle v'w' \rangle^2)^{1/4})$], (f) correlation coefficient for vertical flux of horizontal momentum [$r_{uw} = \langle u'w' \rangle \times (\sigma_u \sigma_w)^{-1}$], (g) streamwise velocity skewness ($Sk_{uh} = \langle u'^3 \rangle \times \sigma_u^{-3}$), (h) vertical velocity skewness ($Sk_w = \langle w'^3 \rangle \times \sigma_w^{-3}$) within and above the canopy up to $z/h = 4$ for the five simulations (NN, WU, MU, SU, and FC). All quantities (with the exception of the skewnesses) are normalized by each case's respective w_m (Table 1). The thin black line marks canopy top $z/h = 1$.

in response to the reduction in U_g and decrease to near zero at all heights for no mean wind (FC). Within the canopy, $\langle u_{*a} \rangle \times w_m^{-1}$ diminishes rapidly with descent into the canopy as canopy drag absorbs horizontal momentum.

Numerous investigations (e.g., Shaw et al. 1988; Brunet et al. 1994; Su et al. 1998) have shown that under near-neutral conditions, turbulence within the canopy is notably more efficient at transporting momentum [$r_{uw} = \langle u'w' \rangle \times (\sigma_u \sigma_w)^{-1} \sim 0.6$] than is turbulence in the surface layer aloft ($r_{uw} \sim 0.4$); however, stability's impact on momentum transport efficiency in the canopy's vicinity has received much less attention. Vertical transport of horizontal momentum is most efficient under NN and WU conditions and decreases with increasing instability

(Fig. 7f). Increasing instability does not influence the height of most-efficient transport (i.e., where r_{uw} peaks, $z/h \sim 0.8$) indicating that even under very unstable conditions, turbulence in the canopy's vicinity remains more organized than in the surface layer above. These results correspond well to the CHATS data (Dupont and Patton 2012a).

As discussed by Leclerc et al. (1991), atmospheric stability has a marked influence on velocity skewness (Figs. 7g,h). Consistent with observations (e.g., Dupont and Patton 2012a), horizontal velocity skewness Sk_{uh} is generally positive in the upper-canopy layers (Fig. 7g). For NN, Sk_{uh} peaks at a value of about 0.75 at a height of $z/h = 0.75$. The magnitude of the maximum Sk_{uh}

diminishes with increasing instability, and the peak shifts upward toward canopy top as the vertical shear of the mean horizontal wind diminishes (Fig. 7a). Within the relatively open trunk space, Sk_{u_h} shifts from positive to negative with increasing instability, which we attribute to the increasing importance of thermal plumes emanating from the surface as the canopy-top vertical shear of the horizontal wind diminishes. Above the canopy, atmospheric stability affects the height at which Sk_{u_h} changes sign, with changes occurring at heights as low as $z/h \sim 1.8$ (WU). Note that Sk_{u_h} is calculated by rotating all velocity fields into the mean-flow direction at canopy top such that spanwise velocity skewness Sk_v is approximately zero for all heights (not shown). Under NN conditions, Sk_w is of opposite sign to Sk_{u_h} and exhibits a vertically broad peak (~ 0.55) near mid-canopy. With increasing instability and decreasing canopy-top shear, this Sk_w peak sharpens in the vertical, weakens in amplitude, and shifts upward to $z/h \sim 0.8$, giving way to a subcanopy peak of nearly equal magnitude but opposite sign that probably results from the increased importance of buoyant plumes emanating from the surface, much like the bottom-up heating case discussed by Moeng and Rotunno (1990).

These skewness results suggest a switch in turbulent transport mechanisms within the canopy as instability increases. In NN and WU, infrequent downward sweeps of high momentum associated with shear-induced “mixing layer” eddies (i.e., $u'_h > 0$ and $w' < 0$) produce positive Sk_{u_h} peaks and negative Sk_w peaks within the canopy. With increasing instability (i.e., reduced vertical shear of the mean horizontal wind at canopy top), small convective plumes originating within the canopy and at the surface take over; these rising, low horizontal velocity events produce negative Sk_{u_h} peaks and positive Sk_w peaks in the lower canopy.

The peak values of Sk_{u_h} and Sk_w shown in Figs. 7g and 7h are slightly smaller than the peak values observed at CHATS (Dupont and Patton 2012a); however, they follow a similar stability-generated trend. Pan et al. (2014a,b) suggest that using a wind speed-dependent drag coefficient (mimicking plant reconfiguration in flexible plant canopies more accurately predicts these third-order moments in canopy LES with limited vertical domain size). However, the inclusion of ABL-scale eddies markedly improves skewness profiles compared to a number of previous canopy LES (e.g., Patton 1997; Su et al. 1998; Patton et al. 2003) even without using a wind speed-dependent drag coefficient.

3) SPECTRA

In the surface layer above the canopy, one expects kinetic energy spectra to generally follow the Kaimal

et al. (1972) spectrum. Su et al. (2004) used long-term data from a tower to modify Kaimal et al.’s (1972) formulations for a wider range of stability conditions above a forest canopy. These two studies (among numerous others) collectively show that spectral peaks shift toward lower frequencies (or wavenumbers) as the atmosphere evolves from neutral toward unstable stability.

Following Sullivan and Patton (2011), Fig. 8 presents one-dimensional power spectra of horizontal and vertical velocity at four heights for two stability conditions (NN and FC). These spectra are calculated by generating two-dimensional power spectra at a given height and averaging in circular rings at constant $k_h = (k_x^2 + k_y^2)^{1/2}$ and over time.

Well above the canopy ($z/h = 10$), spectra for both velocity components and both stabilities generally reveal the expected $-5/3$ slope. As Sullivan and Patton (2011) found, horizontal wind spectra at $z/h = 6$ ($z/z_i \sim 0.1$) peak at lower wavenumbers than do vertical velocity spectra, as horizontal velocity variance amplifies as a result of ABL-scale downdrafts preferentially transferring energy into ABL-scale horizontal motions under the influence of wall blocking (Hunt and Graham 1978), generating two-sloped character of E_u above the canopy.

Compared to spectra near the top of the surface layer and above ($z/z_i > 0.1$), energy at low wavenumbers in NN diminishes as the canopy top is approached through the RSL (i.e., $z/h = 2 \rightarrow 1$); horizontal velocity spectra maintain significant contributions at low wavenumbers, but the spectral peak for vertical velocity shifts to higher wavenumbers. At these heights, increased energy content at canopy-scale wavenumbers ($k_h h = 1$) in NN becomes clearly apparent as the spectra begin revealing the energy associated with eddies generated via the canopy-top inflection-point instability (e.g., Raupach et al. 1996; Finnigan et al. 2009). NN spectra at mid-canopy height ($z/h = 0.5$) maintain a similar shape to those at canopy top (i.e., relatively flat spectra across all wavenumbers out to about $k_h h = 1$) but diminish in magnitude by about a factor of 10 as a result of work performed against canopy-induced form drag.

Under FC conditions, amplification of horizontal velocity variance at low wavenumbers by wall blocking continues all the way down to $z/h = 2$, with very little modification to the energy content at wavenumbers larger than $k_h z_i \sim 30$. At canopy top and within ($z/h = 1$ and 0.5), there is very little canopy-induced modification except for the rapid reduction across all scales at $z/h = 0.5$, corresponding to the reduction of $\sigma_u \times w_m^{-1}$ discussed in Fig. 7a. As in NN, the spectral peak for vertical velocity under FC conditions shifts to larger wavenumbers with descent toward the canopy top and largely remains constant from canopy top to below.

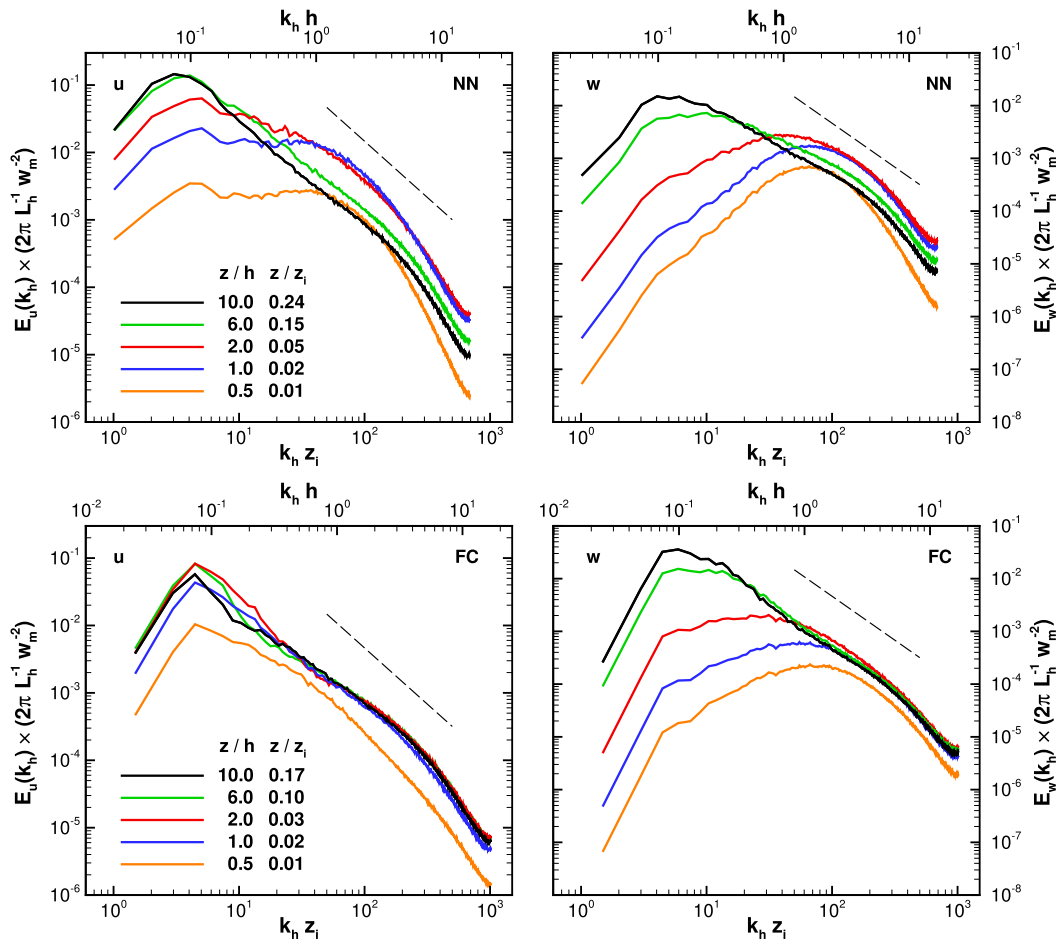


FIG. 8. Two-dimensional normalized energy spectra of (left) horizontal velocity u and (right) vertical velocity w for two stability regimes: (top) NN and (bottom) FC. The spectra are functions of the magnitude of the horizontal wavenumber vector $k_h = |\mathbf{k}|$. Each figure contains spectra at four heights, $z/h = (0.5, 1.0, 2.0, 6.0)$, where approximate values of those heights relative to the ABL depth z_i are also shown. L_h represents the physical size of the largest ring in the circular average (5120 m). The dashed line depicts $k_h^{-5/3}$. Note that the y-axis ranges differ between the u and w figures but are the same between the two different stabilities.

b. Scalars

A unique feature of the simulations discussed here involves the coupling between the turbulence and the within-canopy scalar sources. By incorporating a fully interactive and resolved canopy within simulations permitting full ABL-scale motions, we can investigate the coupling between atmospheric stability variations and canopy scalar exchange.

1) SCALAR SOURCE/SINKS

(i) Instantaneous fields

Horizontal slices of instantaneous sunlit leaf temperature fluctuations θ'_l at $z/h = 0.6$ (the height of maximum plant area density, Fig. 2) contain the signature of ABL-scale organized motions (left panels in Fig. 9) with relatively warm (cool) θ'_l coinciding with narrow (wide)

regions of ABL-scale rising (sinking) motion and weak (strong) horizontal winds (see Figs. 3–6). Interestingly, Katul et al. (1998b) also found the signature of ABL-scale motions in infrared thermometer measurements of θ_l over grass.

This spatial variability in θ_l produces similar spatial structure in the canopy potential temperature and water vapor specific humidity sources S_θ and S_q (middle and right panels in Fig. 9, respectively). Regions of high θ_l largely coincide with regions of low S_θ and high S_q , and vice versa, a feature that can result from a combination of the following: 1) the physiological response of the leaves actively modulating their stomatal resistance r_s to regulate their temperature θ_l and 2) turbulent wind fluctuations enhancing/reducing heat/moisture transport away from the leaves [see Eqs. (11) and (12)]. Because r_s is positively correlated with θ_l (not shown), the positive

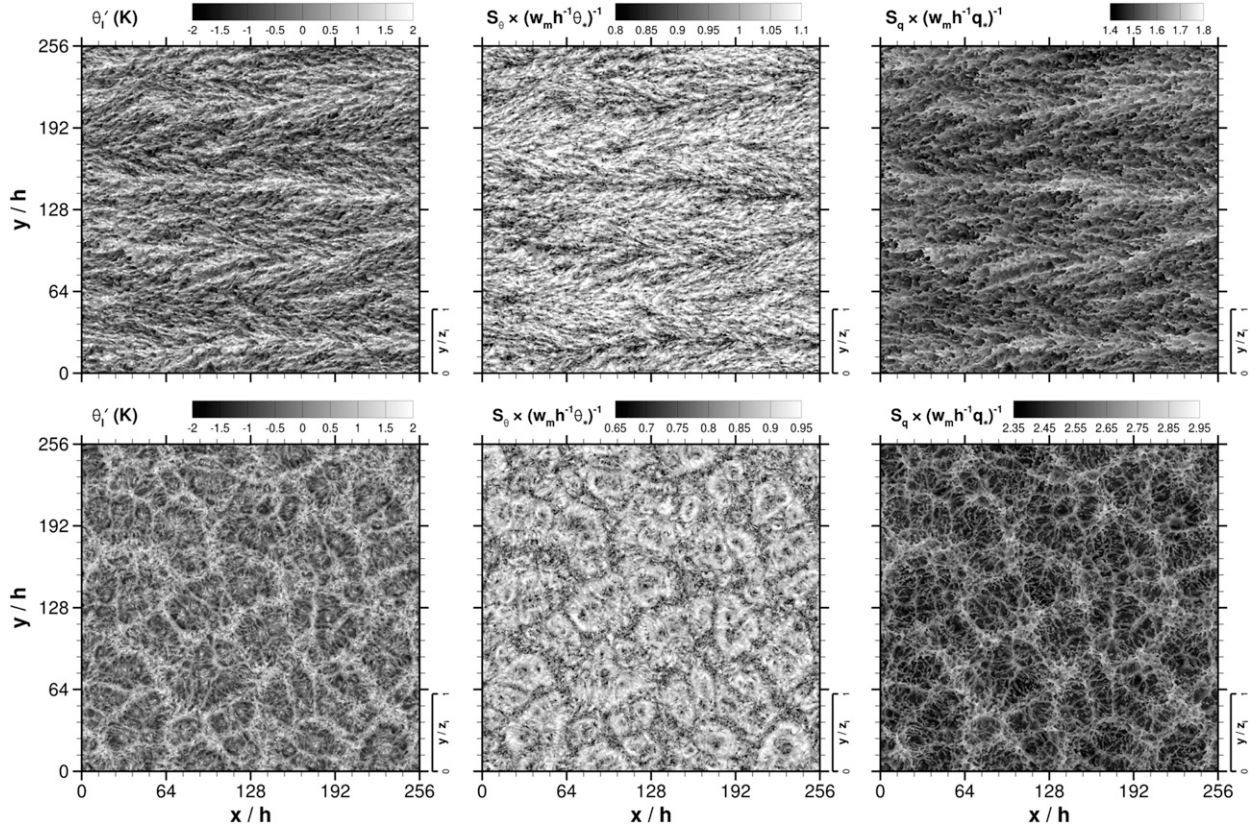


FIG. 9. Instantaneous horizontal slices at $z/h = 0.6$ of normalized (left) sunlit leaf temperature fluctuations θ'_l , (middle) potential temperature source from the canopy S_θ , and (right) water vapor mixing ratio source from the canopy S_q . These quantities are presented for two cases: (top) WU and (bottom) FC. The scalar sources are normalized by the noted combination of each case's w_m , θ_* , and q_* (Table 1) and the canopy height h . Each panel is presented in a coordinate system relative to h ; the small axis at the bottom right of each panel depicts the ABL depth z_i valid for each case.

correlation between θ_l and S_q occurs through q_l and its dependence on θ_l [recall that $q_l = q_{\text{sat}}(\theta_l)$]. Through these links between the biology and the turbulence, canopies spatially segregate S_θ and S_q , which probably contributes to the dissimilar transport between θ and q (e.g., Lemaud and Irvine 2006) and occurs at ABL scales [i.e., notably larger scales than those discussed by Huang et al. (2013)].

Modulation of the heat and water vapor source strengths (S_θ and S_q) by ABL-scale motions also suggests important consequences for averaging times required to close energy and carbon budgets using tower measurements. Because ABL-scale structures can take on the order of 30 min to several hours to advect past a tower, flux measurements could require longer averaging times than generally appreciated in order for the measurement to be representative of the tower's footprint (e.g., Finnigan et al. 2003).

In addition, since some canopies emit reactive gases (e.g., isoprene) according to a combination of a leaf's absorbed radiation and temperature (e.g., Guenther et al. 1993), ABL-scale modulation of leaf temperature

θ_l suggests that the interaction between ABL-scale turbulence and leaf-level exchange segregates reactant emissions that may influence reaction rates throughout the entire ABL.

(ii) Mean source/sink profiles and their standard deviation

The temporally and spatially varying scalar source distributions (Fig. 9) permit investigation into the influence of atmospheric stability on canopy scalar source statistics. For all stabilities, $\langle S_\theta \rangle$ peaks at a greater height within the canopy ($z/h \sim 0.75$) than does $\langle S_q \rangle$ ($z/h \sim 0.55$; see Figs. 10a and 10e), where the peak of $\langle S_\theta \rangle$ occurs at the location with highest incoming shortwave radiation absorption just above the PAD maximum, and the peak of $\langle S_q \rangle$ sits just below the PAD maximum where the light regime is dominated by scattered shortwave radiation absorption. Note that $\langle S_q \rangle$ responds more to atmospheric stability variations than does $\langle S_\theta \rangle$, with enhanced moisture sources occurring at the stability extremes (i.e., NN and FC). As a reference, $\langle r_b \rangle = (0.05, 0.06, 0.07, 0.08,$

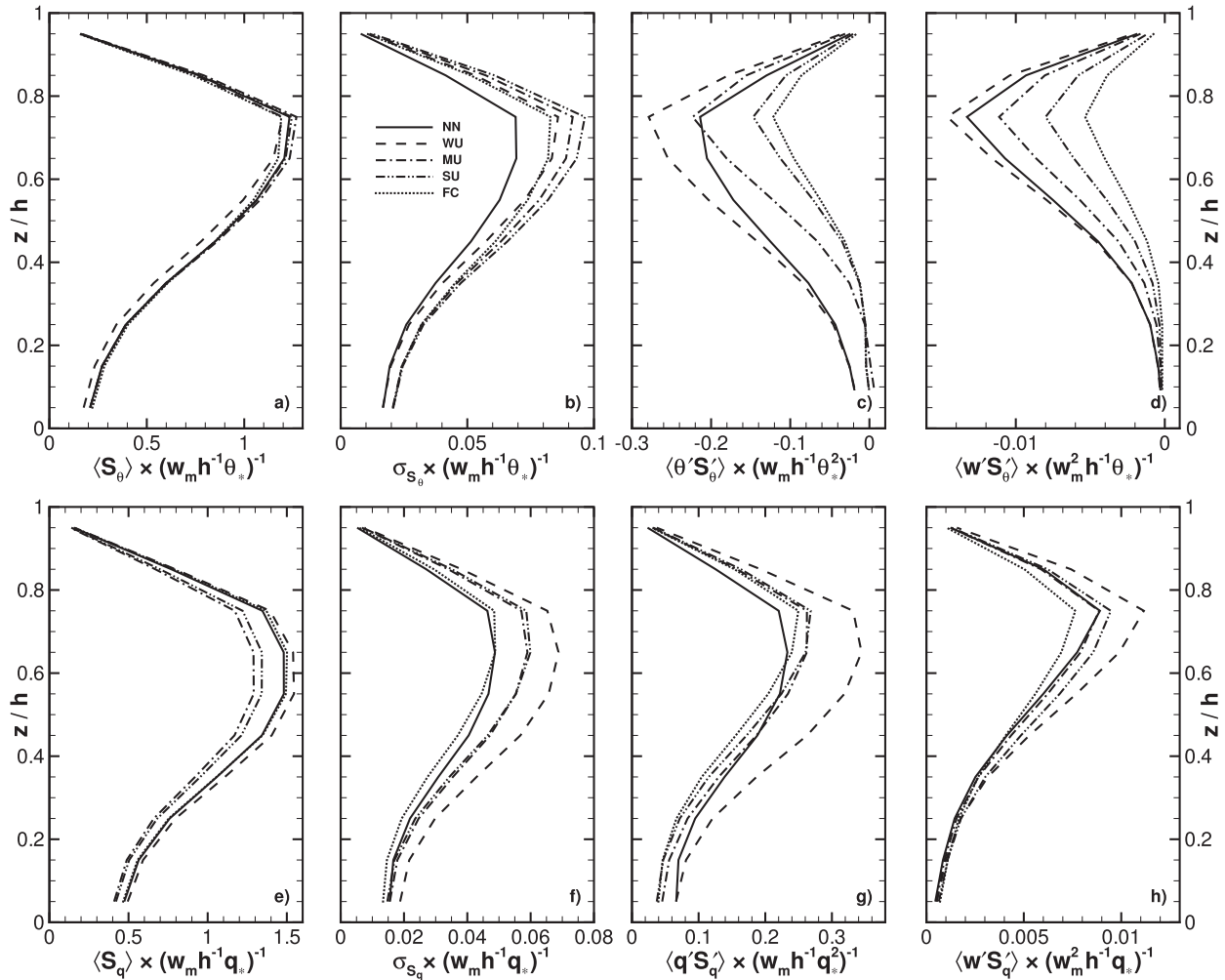


FIG. 10. (top) Horizontal- and time-averaged vertical profiles of normalized (a) potential temperature source per grid volume $\langle S_\theta \rangle$, (b) standard deviation of the potential temperature source per grid volume ($\sigma_{S_\theta} = \langle S_\theta^2 \rangle^{1/2}$), (c) spatial covariance of the potential temperature source with potential temperature $\langle \theta' S_\theta \rangle$, and (d) spatial covariance of the potential temperature source with vertical velocity $\langle w' S_\theta \rangle$ within and above the canopy up to $z/h = 4$ for the five simulations (NN, WU, MU, SU, and FC). (bottom) As in (top), but for water vapor mixing ratio. Each quantity is normalized by the noted combination of each case's w_m , θ_* , and q_* (Table 1) and the canopy height h . The thin black line marks canopy top $z/h = 1$.

$0.08) \text{ s mm}^{-1}$, and $\langle r_s \rangle = (3.28, 1.83, 2.74, 2.76, 3.30) \text{ s mm}^{-1}$ at $z/h = 0.65$ for cases (NN, WU, MU, SU, FC), respectively.

Vertical profiles of scalar source standard deviations (Figs. 10b,f) peak at similar heights to those of their respective mean. For these simulations, σ_{S_θ} reaches as high as 10%–12% of $\langle S_\theta \rangle$, while σ_{S_q} is only about 1% of $\langle S_q \rangle$. This difference between the variability of heat versus moisture sources largely results from 1) the GEM's (Niyogi et al. 2009) imposed time lag on stomatal resistance's response to fluctuating water vapor gradients, 2) the stomatal resistance's dominance over the total resistance, and 3) the fact that the stomatal resistance varies by only about 4% about the mean, whereas the boundary layer resistance varies by nearly

40% (not shown). The relative amplitudes of these scalar source fluctuations likely vary with soil moisture availability but as presented can be used to guide expected spatial variability when implementing multilevel canopy models within a weather or climate model that cannot resolve turbulence structure (e.g., Falk et al. 2014).

(iii) Production/loss of scalar variance and flux

The temporally and horizontally averaged equations for resolved-scale scalar variance (flux) in the presence of temporally and spatially varying scalar sources contain correlations between the scalar (vertical velocity) and the source (e.g., Finnigan 1985). For any scalar c , these correlations appear on the right-hand side of the equations as

$$\frac{1}{2} \frac{\partial \langle c'^2 \rangle}{\partial t} = \dots + \langle c' S'_c \rangle \quad \text{and} \quad (16)$$

$$\frac{\partial \langle w' c' \rangle}{\partial t} = \dots + \langle w' S'_c \rangle. \quad (17)$$

See Patton et al. (2001) for the complete scalar variance and flux budget equations. In the situation where scalar sources are imposed and constant, these source correlation terms do not appear. The questions to be addressed here are 1) how important are these terms when the canopy can respond to local atmospheric demand? and 2) how do these covariances contribute to the production/destruction of resolved-scale scalar variance or flux?

For the current simulations, potential temperature fluctuations in the canopy air space are generally negatively correlated with leaf-level potential temperature sources (Fig. 10c), while water vapor fluctuations are positively correlated with leaf-level water vapor sources (Fig. 10g). According to Eq. (11), regions of high potential temperature coincide with low S_θ when boundary layer resistance r_b is high and/or when leaf temperature θ_l is high; both of these scenarios are likely when the local scalar wind speed is low. The organized ABL-scale structures create regions of strong divergence and convergence (Figs. 5 and 6), which are associated with relatively weak winds; low winds are ineffective at transporting heat away from the leaves (high r_b), resulting in regions of low S_θ (Fig. 9). The organized ABL-scale structures also generate regions with high wind speed fluctuations u'_h , which—in these simulations where the canopy is generally water-limited with high r_s —create regions of reduced r_b producing high S_θ at the expense of S_q .

In a broad sense, $\langle \theta' S'_\theta \rangle$ decreases with increasing instability, while $\langle q' S'_q \rangle$ is smallest at the end-member stability classes and transitions to larger values at intermediate stabilities, which probably results from r_b varying solely with wind speed, while r_s responds to physiological control. The terms $\langle w' S'_\theta \rangle$ and $\langle w' S'_q \rangle$ follow a similar trend, revealing the tight coupling between the respective sources and both the local wind and scalar fields.

Examining the percent contributions of the correlation terms in Eqs. (16) and (17) relative to the total variance or flux production quantifies the importance of these terms; Table 5 presents these ratios evaluated at $z/h = 0.65$. At this height, the correlation terms for scalar variance contribute a maximum of 5.6% (7.2%) of the total variance for θ (q), with a general trend that the contribution from $\langle \theta' S'_\theta \rangle$ ($\langle q' S'_q \rangle$) tends to decrease (increase) with increasing instability. Compared to the contribution of the source correlation terms for variance, the source correlation terms for vertical scalar flux

TABLE 5. The percentage magnitude of the correlation terms in Eqs. (16) and (17) relative to the total variance or flux production [i.e., $R_{\langle c' S'_c \rangle} = 100 \times |\langle c' S'_c \rangle| / |\langle w' c' \rangle (\partial(c)/\partial z)|$, and $R_{\langle w' S'_c \rangle} = 100 \times |\langle w' S'_c \rangle| / |\langle w'^2 \rangle (\langle \partial c \rangle / \partial z) + (g/\theta v_*) \langle \theta' c' \rangle|$, where c represents either θ or q] at $z/h = 0.65$.

Case	$R_{\langle \theta' S'_\theta \rangle}$	$R_{\langle q' S'_q \rangle}$	$R_{\langle w' S'_\theta \rangle}$	$R_{\langle w' S'_q \rangle}$
NN	4.6	4.6	1.1	0.9
WU	5.6	6.8	1.2	1.6
MU	3.8	6.8	1.0	2.4
SU	2.8	7.2	0.8	3.3
FC	2.4	5.0	0.7	2.7

reveal a similar trend with increasing stability with a greater overall contribution for q compared to θ . The percentage contribution of these terms varies with height and becomes increasingly more important in regions where scalar variance and/or flux production are small (e.g., in the subcanopy's relatively open trunk space; not shown).

2) SCALAR STATISTICS

Vertical profiles of normalized $\langle \theta \rangle$ and $\langle q \rangle$ minus each simulation's respective canopy-top value ($\langle \theta \rangle_h$ and $\langle q \rangle_h$) are presented in Figs. 11a and 11e. Scaling by θ_* or q_* removes source strength variations across the simulations and allows one to assess variations in profile shapes resulting from differences in vertical mixing and dispersion. However, the scalar profiles are also influenced by the entrainment of free-tropospheric air from above the ABL. Alternative scalings incorporating the influence of entrainment on the profiles were considered (e.g., Moene et al. 2006); however, the current scaling was ultimately selected because of the difficulty in observing entrainment fluxes from surface-based towers. Therefore, the important information conveyed by Figs. 11a and 11e lies in the profile shapes and vertical gradients of $\langle \theta \rangle$ and $\langle q \rangle$.

Above the canopy ($z/h > 2$), $\langle \theta \rangle$ and $\langle q \rangle$ become more well mixed as buoyancy becomes increasingly important. Vertical scalar gradients at canopy top are similar across all stabilities and both scalars. Compared to $\langle \theta \rangle$, $\langle q \rangle$ in the subcanopy ($z/h < 0.5$) becomes increasingly well mixed, with increasing instability resulting from changes in the turbulence and the S_q profile. The fact that temperature is not as well mixed in the subcanopy as humidity can likely be explained by the differing relative magnitudes of their surface sources (Table 1).

Even though vertical scalar gradients vary little at canopy top with transition from NN to FC (Figs. 11a,e), scalar standard deviations (σ_θ and σ_q) and skewness (Sk_θ and Sk_q) at canopy top vary substantially (Fig. 11). Previous research has documented the influence of

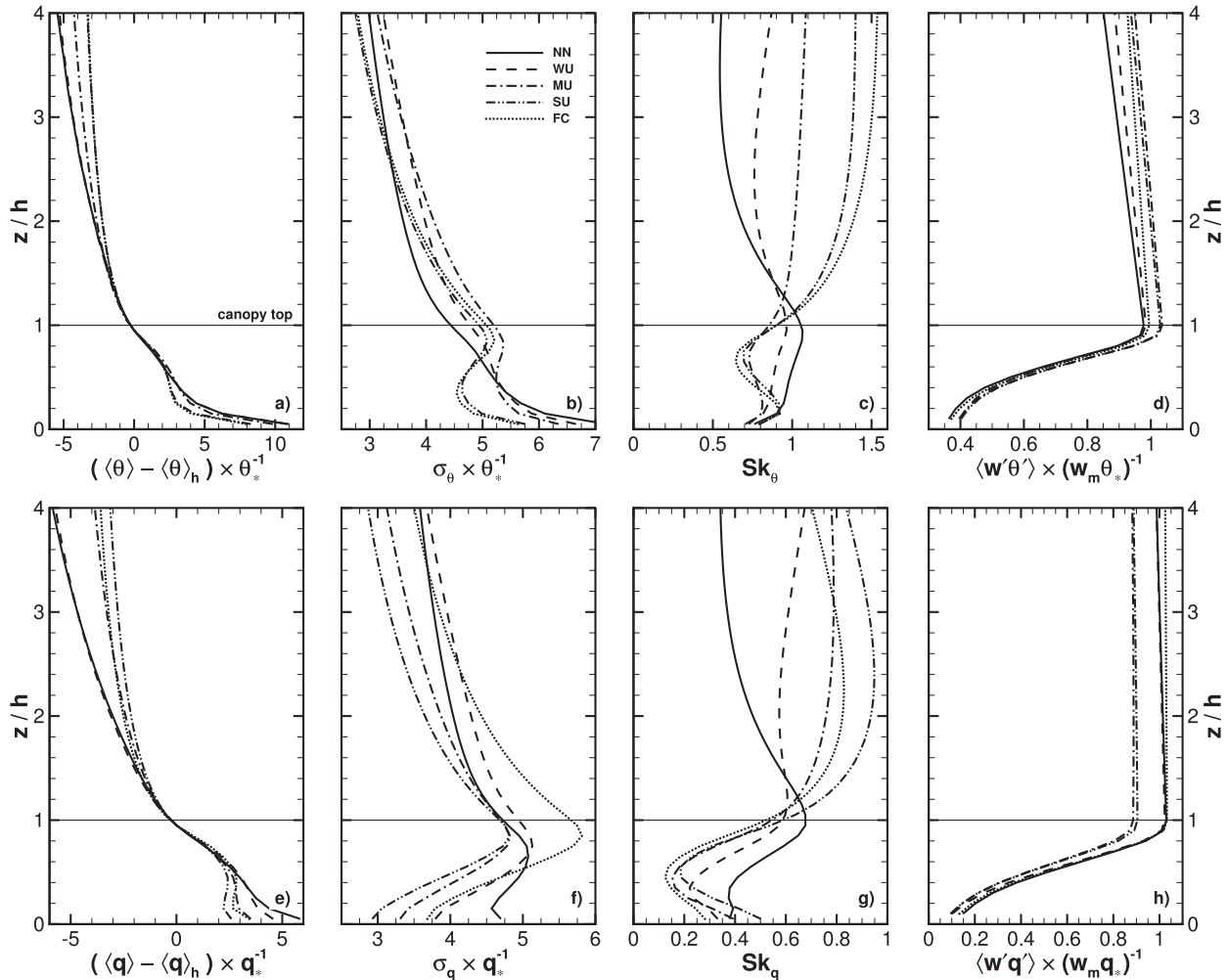


FIG. 11. (top) Horizontal- and time-averaged vertical profiles of (a) the normalized potential temperature $\langle \theta \rangle$ deviation from the canopy-top mean $\langle \theta \rangle_h$, (b) the normalized standard deviation of potential temperature ($\sigma_\theta = (\theta'^2)^{1/2}$), (c) potential temperature skewness ($Sk_\theta = \langle \theta'^3 \rangle / \sigma_\theta^3$), and (d) normalized vertical turbulent flux of potential temperature $\langle w'\theta' \rangle$ within and above the canopy up to $z/h = 4$ for the five simulations (NN, WU, MU, SU, and FC). (bottom) As in (top), but for water vapor mixing ratio. All quantities (with the exception of the skewnesses) are normalized by the noted combination of each case's θ_* , q_* , and w_m (Table 1). The thin black line marks canopy top $z/h = 1$.

ABL-scale downwelling motions bringing free-tropospheric air down to the surface (e.g., Deardorff 1972; Schmidt and Schumann 1989; Patton et al. 2005). Mahrt (1991), Couvreux et al. (2007), and van de Boer et al. (2014) discussed these downwelling events and their impact on near-surface scalar statistics (variance, skewness, and flux). Couvreux et al. (2007) showed that dry tongues of air entrained from the free troposphere produce negative q skewness in the upper ABL. On the other hand, potential temperature $\langle \theta \rangle$ increases with height above the ABL, typically resulting in positive Sk_θ in the middle to upper ABL (e.g., Lenschow et al. 1994). Near the surface (below $z/z_i \sim 0.2$), Couvreux et al. (2007) found that Sk_q can be both positive and negative

depending on the ratio of entrainment-to-surface flux, in accordance with Mahrt (1991). For weak-wind, convectively unstable cases, Mahrt (1991) found that upon reaching the warm moist surface, ABL-scale downdrafts tended to be dryer but not warmer than surrounding warm moist updrafts. However, in windier near-neutral cases, Mahrt (1991) found that ABL-scale dry downdrafts were less likely to reach the surface without major modification resulting in positive near-surface Sk_q as upward motions dominate.

The influence that these ABL-scale motions have on canopy-top scalar moments can be seen in Fig. 11. Above-canopy scalar skewness profiles are positive and generally increase with increasing instability (Figs. 11c,g);

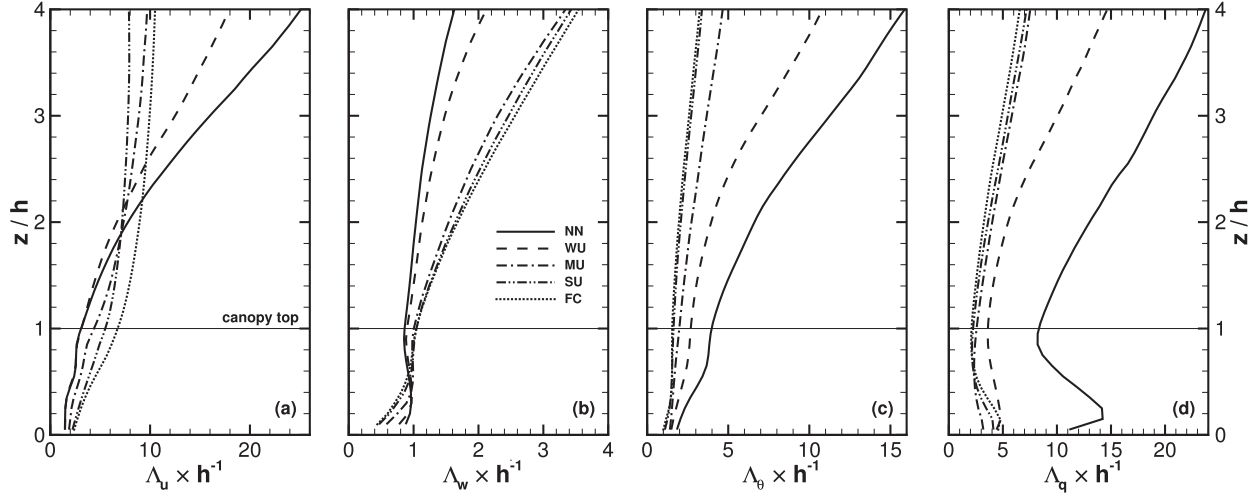


FIG. 12. Streamwise integral length scales of (a) streamwise velocity Λ_u , (b) vertical velocity Λ_w , (c) temperature Λ_θ , and (d) water vapor mixing ratio Λ_q normalized by the canopy height h .

however, above-canopy Sk_q only increases up to SU and then diminishes for FC. Inspection of Sk_θ and Sk_q profiles through the ABL reveals increasingly positive Sk_θ and negative Sk_q through the ABL with increasing instability (not shown). Therefore, ABL-scale downward transport of unmodified dry air increases with increasing instability such that the canopy-source-generated positive Sk_q skewness transitions toward negative values at increasingly lower heights above the canopy (but at heights above those shown in Fig. 11g).

c. Spatial integral length scales

To calculate integral length scales from single-point tower measurements, Taylor's hypothesis is required to convert integral time scales to length scales (e.g., Baldocchi and Meyers 1988). However, Taylor's hypothesis requires $\sigma_u/\langle u_h \rangle \ll 1$, which is generally not met within or above a canopy (Fig. 7). As an alternative, Shaw et al. (1995) used two-point hot-wire measurements to directly measure length scales in a neutral wind tunnel canopy flow and found them to be approximately 2.5–3 times larger in the canopy's vicinity ($z/h < 2$) than their Eulerian counterpart; Su et al. (2000) found similar results in a neutral LES. Probably resulting from the costs and difficulty in collecting spatially varying field observations, there is very little information concerning stability influences on length scales within and above outdoor canopies. Therefore, we now discuss integral length scales computed from the current set of simulations. In what follows, each variable's integral length scale Λ_χ of variable χ is calculated as the time average of the horizontal separation at which the instantaneous autocorrelation function falls to e^{-1} (e.g., Kaimal and Finnigan 1994).

Under NN conditions, streamwise integral length scales for streamwise velocity Λ_u at canopy top are about $3h$ (Fig. 12a), which is directly comparable to that found by Shaw et al. (1995) in the wind tunnel. Within the canopy, Λ_u diminishes slightly, dropping as low as about $1.5h$ near the underlying surface. At $z/h = 0.5$, Λ_u is about $2h$, which also matches the results of Shaw et al. (1995). Above the canopy, Λ_u immediately begins increasing with height and reaches about $25h$ at $z/h = 4$; while Shaw et al. (1995) found Λ_u to be nearly constant with height between $1 < z/h < 4$. This discrepancy clearly results from the large ABL-scale elongated roll-like structures presented in Figs. 3–6 that are absent in Shaw et al.'s (1995) wind tunnel data. The value of Λ_u at canopy top increases with increasing instability, reaching about $7h$ in FC. Compared to NN, Λ_u also increases within the canopy with increasing instability but only increases to about $2.4h$ near the surface in FC. With the transition from ABL-scale rolls to cells when transitioning from NN to FC conditions (Figs. 3–6), above-canopy Λ_u changes character such that Λ_u increases for all cases (but at a diminishing rate) up to $z/h \sim 2$. Above $z/h = 2$, Λ_u continues to increase, but at an even slower rate than $1 < z/h < 2$.

In NN conditions, streamwise integral length scales for vertical velocity Λ_w are nearly constant with height at a value of about h (i.e., canopy scale) from the surface up to approximately $z/h = 3$ (although at canopy top, Λ_w diminishes slightly to about $0.85h$; Fig. 12b); note that in the absence of the canopy, one would expect Λ_w to increase almost linearly with distance above the surface (e.g., Wyngaard 2010), so the nearly constant Λ_w up to $z/h = 3$ clearly results from canopy-scale eddies generated by the inflection-point instability at canopy top

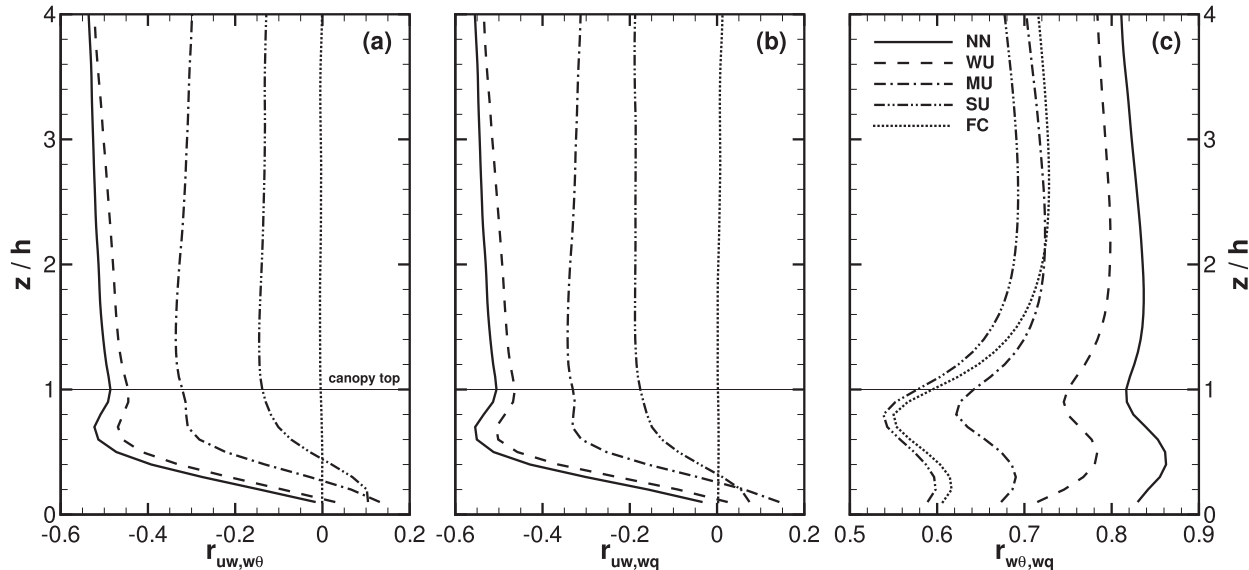


FIG. 13. Vertical profiles of the correlation coefficient between (a) the vertical flux of streamwise momentum and vertical potential temperature flux $r_{uw,w\theta}$, (b) the vertical flux of streamwise momentum and vertical water vapor mixing ratio flux $r_{uw,wq}$, and (c) the vertical potential temperature flux and vertical water vapor mixing ratio flux $r_{w\theta,wq}$ for all five stability regimes. The thin solid line marks canopy top $z/h = 1$.

(e.g., Raupach et al. 1996; Finnigan et al. 2009). With increasing influence of buoyancy, Λ_w in the subcanopy ($z/h < \sim 0.5$) diminishes systematically (toward a value of about $0.4h$ at the surface in FC), which reflects the decreasing importance of canopy-scale eddies generated by the canopy-top inflection-point instability and an increasing importance of buoyant plumes emanating from the underlying surface. Increasing instability produces little change in Λ_w at canopy top (although Λ_w increases slightly to about $1h$), but it produces noticeable increases in Λ_w above the canopy (reaching values of about $3.5h$ at $z/h = 4$ in FC), reflecting the increasingly important coalescence of buoyant plumes emanating from levels below.

Scalar streamwise integral length scales diminish at all levels with increasing instability (Fig. 12c,d). In general, both Λ_θ and Λ_q are larger than Λ_w , and Λ_q is about twice as large as Λ_θ , which matches Couvreux et al.'s (2005) findings in simulations of the IHOP_2002 field campaign. Important in this discussion is that de Roode et al. (2004) showed that large Λ_q compared to Λ_θ could be explained by differing ratios of the surface to entrainment flux between the two scalars, which results in variance spectra for q peaking at much larger scales than θ .

d. Momentum and scalar flux correlation

Katul et al. (1997) noticed that the ejection/sweep cycles for momentum and scalars are closely coupled but not identical. Using single-point measurements above a vineyard and a lake, Li and Bou-Zeid (2011) showed that the correlation between momentum and scalar (temperature and water vapor) fluxes decreases with

transition from neutral to unstable conditions, and they put forward a hypothesis that this results from an evolution from hairpin structures to thermal plumes occurring across the evolution of atmospheric stability. Using vertical profiles from the CHATS field campaign [within and above a walnut orchard (Patton et al. 2011)], Dupont and Patton (2012b) also found the correlation between momentum and scalar fluxes to decrease with increasing instability but noted that the correlations were 1) nearly independent of height above the canopy, but within the canopy they decreased toward zero near the ground; and 2) largest when the trees were in full leaf because of collocation of the primary momentum sink and scalar sources in the canopy. Important in both of those investigations (Li and Bou-Zeid 2011; Dupont and Patton 2012b) is that they hinged on time-averaged statistics.

The simulations discussed here provide an opportunity to evaluate Li and Bou-Zeid's (2011) hypothesis. Figure 13 presents vertical profiles of correlation coefficients between momentum and scalar fluxes $r_{uw,w\phi}$ and between potential temperature and water vapor fluxes $r_{w\theta,wq}$, which are defined as

$$r_{uw,w\phi} = \frac{\langle (u'w' - \langle u'w' \rangle)(w'\phi' - \langle w'\phi' \rangle) \rangle}{\sigma_{uw}\sigma_{w\phi}} \quad \text{and} \quad (18)$$

$$r_{w\theta,wq} = \frac{\langle (w'\theta' - \langle w'\theta' \rangle)(w'q' - \langle w'q' \rangle) \rangle}{\sigma_{w\theta}\sigma_{wq}}, \quad (19)$$

where ϕ is either the atmospheric potential temperature θ or specific humidity q , and σ_{uw} and $\sigma_{w\phi}$ are the standard deviations of $u'w'$ and $w'\phi'$, respectively.

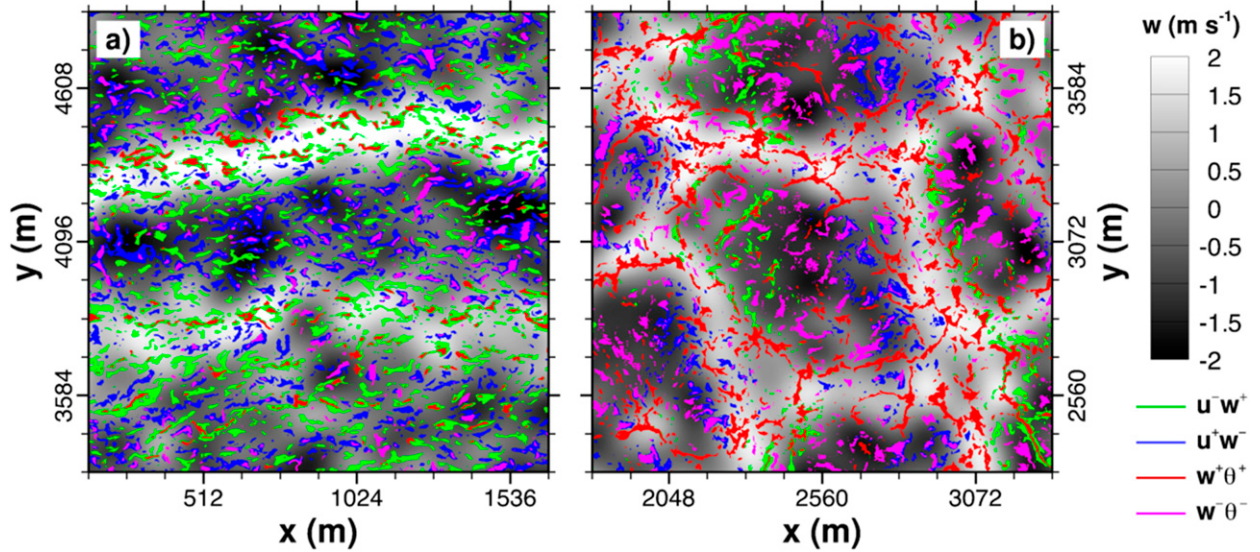


FIG. 14. Instantaneous horizontal slices of low-pass-filtered vertical velocity at $z/h = 6$ (grayscale) from (a) WU and (b) FC. Regions of negative $u'w'$ and positive $w'\theta'$ at canopy top ($z/h = 1$) and broken down by quadrants are overlaid in color. Using notation such that for any variable χ , χ^+ signifies $\chi' > 0$ and χ^- signifies $\chi' < 0$, green regions depict u^-w^+ , blue regions depict u^+w^- , red regions depict $w^+\theta^+$, and pink regions depict $w^-\theta^-$. In (a), only regions with $[u^-w^+, u^+w^-]$ more negative than $[-1, -1] \text{ m}^2 \text{s}^{-2}$ and $[w^+\theta^+, w^-\theta^-]$ larger than $[1, 1] \text{ m K s}^{-1}$ are shown. In (b), only regions with $[u^-w^+, u^+w^-]$ more negative than $[-0.3, -0.4] \text{ m}^2 \text{s}^{-2}$ and $[w^+\theta^+, w^-\theta^-]$ larger than $[0.4, 0.3] \text{ m K s}^{-1}$ are shown.

Under NN conditions, momentum and scalar fluxes are generally negatively correlated above the canopy (Figs. 13a,b); that is, upward motions typically carry low horizontal momentum and high scalar fluxes, with the opposite for downward motions. Consistent with Li and Bou-Zeid (2011) and Dupont and Patton (2012b), the magnitude of $r_{uw,w\phi}$ above the canopy diminishes with increasing instability and is nearly constant with height. Within the canopy, the magnitude of $r_{uw,w\phi}$ diminishes rapidly with decreasing height, becoming positive near the surface for all cases. The correlation coefficients between the two scalar fluxes $r_{w\theta,wq}$ are greater than 0.8 under NN conditions and also diminish with increasing instability, especially in the canopy's vicinity, where, in the most unstable cases, $r_{w\theta,wq}$ falls as low as 0.55 near canopy top and to about 0.6 in the subcanopy.

It is extremely difficult to ascertain the linkage between ABL-scale motions and canopy-top exchange and their control over these correlations using single-point-based (Li and Bou-Zeid 2011) or single-tower-based measurements (Dupont and Patton 2012b). To this end, Fig. 14 presents instantaneous horizontal slices of vertical velocity at $z/h = 6$ (grayscale) for a $1536 \times 1536 \text{ m}^2$ subset of the domain for cases WU and FC. Overlaid on the grayscale image are quadrant analyses (e.g., Wallace et al. 1972; Willmarth and Lu 1972) of momentum and potential temperature flux at canopy top ($z/h = 1$; colors); only sweep/ejection phases are presented where the notation is such that for any variable χ , χ^+ signifies $\chi' > 0$ and χ^- signifies $\chi' < 0$.

Looking at Fig. 14, one can immediately notice that the ABL-scale structures organize exchange at canopy top. In Fig. 14a, canopy-top regions of u^-w^+ more negative than $-1 \text{ m}^2 \text{s}^{-2}$ (ejections; green) predominantly coincide with canopy-top regions of $w^+\theta^+$ larger than 1 m K s^{-1} (red), and locations where they coincide largely occur at the edges of the ABL-scale updrafts at $z/h = 6$, while regions of u^+w^- (sweeps; blue) tend to occur coincidental with regions $w^-\theta^-$ and are largely located underneath regions of ABL-scale downdraft.

Figure 14b shows that canopy-top momentum and scalar exchange occurs quite differently when there is no mean shear. ABL-scale updrafts (downdrafts) create regions of convergence (divergence) beneath them at canopy top. These regions of convergence and divergence generate near-surface horizontal winds acting as the near-surface component of a closed ABL-scale circulation, thereby spatially separating regions of u^+ and u^- at canopy top such that regions of large magnitude u^-w^+ typically occur in regions where the ABL-scale winds are in the negative x direction (green) and u^+w^- in regions where the ABL-scale winds are in the positive x direction (blue). For scalars, warm air is largely transported upward ($w^+\theta^+$; red) in regions beneath the ABL-scale updrafts, and cooler air is transported downward ($w^-\theta^-$; pink) beneath the ABL-scale downdrafts. Thus, this analysis supports the idea that the evolution of ABL-scale structures with stability spatially shifts the regions where momentum and scalar fluxes

occur and produces the correlation variations discussed by Li and Bou-Zeid (2011) and Dupont and Patton (2012b) and presented in Fig. 13. The finding that ABL-scale structure spatially controls turbulence at canopy top is also consistent with Katul et al.'s (1998a) indirect observational evidence suggesting that scalar fluxes near canopy top occur via eddies of similar size to those contributing to above-canopy σ_w . These results suggest that canopy turbulence parameterizations for models unable to resolve the canopy need to incorporate an additional length and/or time scale associated with the ABL-scale organized motions, a suggestion not terribly dissimilar to that put forward by Wesson et al. (2003).

7. Conclusions

Aspects of atmospheric stability's influence on ABL-scale structure and its impact on canopy exchange have been investigated by analyzing results from five large-eddy simulations of ABLs interacting with a resolved and interactive broadleaf forest canopy. To perform these simulations, a multilevel canopy version of Noah was developed; its basis and implementation are briefly described. The multilevel canopy model allows for the coupled interaction between the turbulent atmosphere and the scalar source distribution (and vice versa)—an essential feature, especially when studying the range of atmospheric stabilities under investigation here.

Key findings arising from analyzing the simulation data include the following:

- ABL-scale structure maintains and imposes its signature at canopy top (especially for streamwise velocity u), creating regions where high-momentum fluid is brought down to canopy top (or low-momentum fluid is ejected from the canopy) at scales tied to the ABL depth, which modifies the horizontal distribution of vertical shear of the horizontal wind at canopy top and places controls on canopy exchange of momentum and scalars.
- Increasing instability reduces mean canopy-top vertical shear of the horizontal wind. As a result, velocity variance, momentum stress, and transport efficiency systematically diminish with increasing instability and importance of buoyant plumes. With transition to free convection, canopy-top velocity skewness values reduce in magnitude but maintain the same sign as found under near-neutral conditions; velocity skewness profiles also transition toward their surface-layer values at lower elevations above the canopy and change sign in the lower canopy as buoyant plumes emanating from the surface become increasingly important.
- Because of the relatively rapid response time of the leaves, organized ABL-scale structures interact with

the plant physiology to generate spatially varying leaf temperatures and scalar sources. Potential temperature sources peak above the level of maximum canopy density, while water vapor specific humidity sources peak just below. Standard deviations of the potential temperature source are as large as about 10% of the source strength, while those for water vapor are only about 1%. Spatially varying sources generate additional terms in the equations for resolved-scale scalar variance and flux. For variances, $\langle \theta' S'_\theta \rangle$ acts to reduce within-canopy potential temperature fluctuations, while $\langle q' S'_q \rangle$ acts to produce water vapor mixing ratio fluctuations; the same is true for $\langle w' S'_w \rangle$ and $\langle w' S'_q \rangle$ for scalar fluxes. The sign and magnitude of these terms contributing to scalar variance and flux are most certainly dependent on soil moisture availability.

- Increasing instability from near neutral to free convection decreases vertical scalar gradients above the canopy and increases scalar variances and scalar skewness. ABL-scale downwelling motions bring dry air to increasingly lower altitudes with increasing instability impacting above-canopy scalar statistics. Increasing instability also reduces within-canopy scalar skewness as the importance of shear-driven canopy-scale motions diminishes.
- Momentum and scalar length scales in the vicinity of the canopy reflect the influence of atmospheric stability and the organized ABL-scale motions. At canopy top, Λ_u increases from about $2h$ for near neutral conditions to about $8.5h$ for free-convective conditions; but, well above the canopy ($z/h > 2$), Λ_u increases much more rapidly in near-neutral conditions than it does under free-convective conditions as ABL-scale motions transition from cells to rolls. Below $z/h = 3$, Λ_w is nearly constant with height at a value of about $1h$ under near-neutral conditions but rapidly increases above the canopy with a transition to free convection, suggesting the continual coalescence of finescale plumes into larger and larger updrafts. Near canopy top, scalar length scales are notably larger than Λ_w and shrink with increasing instability.
- The evolution of ABL-scale structures with atmospheric stability (i.e., the transition from rolls to cells as stability varies from near neutral to free convection) spatially separates momentum and scalar fluxes, which explains their decreasing correlation with increasing instability.

In combination, our analysis confirms the hypothesis that the evolution of ABL-scale organized turbulent motions across stability variations from near neutral to free convection significantly alters turbulent exchange

at the canopy–atmosphere interface. In particular, the evolution of spatial integral length scales and the evolution of spatial separation of momentum and scalar exchange with buoyancy suggest that, in order to transition from near-neutral to free-convective conditions, currently available parameterizations of roughness sublayer turbulence hinging on the shear-induced hydrodynamic instability at canopy top need to incorporate an additional length and/or time scales associated with the ABL-scale organized motions.

The coupled canopy–atmosphere system also shows that the evolution of ABL-scale organized turbulent motions across variations in stability can link with the underlying biologically controlled scalar source/sinks to segregate heat and moisture sources contributing to dissimilarity in their vertical transport—a result that implies that tower-based observations need to be averages over time scales associated with ABL-scale motions (as opposed to canopy-scale motions) when designing measurement strategies to evaluate energy or carbon budgets.

Acknowledgments. We would like to acknowledge Alex Guenther, Fei Chen, Anil Kumar, Peter Harley, Ian Harman, Ray Leuning, Bill Massman, Laurent Perret, and Rich Rotunno, who provided some of the initial code base used to create this multilayer canopy system, contributed the HRLDAS-derived initial soil conditions, and/or offered suggestions along the way. We also thank Arnold Moene and two anonymous reviewers for substantial suggestions/commentary, from which the manuscript benefited greatly.

Support for this project came largely from the Army Research Office (Grant W911NF-09-1-0572) courtesy of Dr. Walter Bach, from the Bio–Hydro–Atmosphere Interactions of Energy, Aerosols, Carbon, H₂O, Organics and Nitrogen (BEACHON) program at NCAR, and through the Center for Multiscale Modeling of Atmospheric Processes (CMMAP) at Colorado State University, NSF Grant ATM-0425247 and Contract G-3045-9 to NCAR. Numerous collaboration visits sponsored by NCAR and CSIRO were an essential aspect of this effort. Additionally, this research would not have been possible without the high-performance computing support from: 1) Yellowstone (ark:/85065/d7wd3xhc) provided by NCAR’s Computational and Information Systems Laboratory, sponsored by the National Science Foundation, and 2) the National Energy Research Scientific Computing Center, a DOE Office of Science User Facility supported by the Office of Science of the U.S. Department of Energy under Contract DE-AC02-05CH11231.

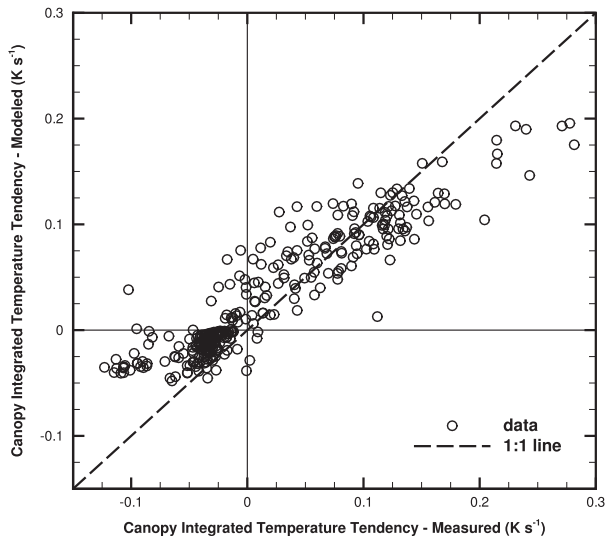


FIG. A1. A test of the multilayer canopy model. Here, the multilayer canopy model is driven by within-canopy vertical profiles of 5-min-averaged observations taken during the final month of the CHATS field campaign (Patton et al. 2011). Presented is a comparison of measured vs modeled portions of a horizontally averaged thermodynamic heat budget vertically integrated over the canopy depth [Eq. (A1)]; if the measurements and the model were perfect, all points would lie on the 1:1 line (long dashed).

APPENDIX

Multilayer Canopy Model: Test against Observations

The new multilevel canopy model is not intended to represent all leaf-level processes and their atmospheric coupling. Rather, it is intended to provide sufficient realism to investigate the importance of leaf-level processes on turbulence–canopy coupling.

The new multilevel canopy model is tested against field observations from the 30-m tower at CHATS (Patton et al. 2011). The CHATS tower included seven levels of winds, temperature, and specific humidity characterizing the within-canopy structure of mean and turbulent quantities within and above a deciduous Chandler walnut orchard (Dupont and Patton 2012a,b). The CHATS tower also included observations of above-canopy four-component radiation, soil temperature and moisture profiles, and soil heat flux. The CHATS campaign took place over a 3-month period, where the final month sampled the canopy layers while the deciduous walnut canopy was in full leaf. See Patton et al. (2011) for more complete details regarding CHATS.

A horizontally averaged, time-averaged, and vertically integrated thermodynamic heat budget can be written as follows:

$$\underbrace{\int_0^h \left(\frac{\partial \langle \theta \rangle}{\partial t} + \frac{\partial \langle w' \theta' \rangle}{\partial z} \right) dz}_{\text{Measured}} = \underbrace{\int_0^h \langle S_\theta \rangle dz}_{\text{Modeled}}, \quad (\text{A1})$$

where θ is potential temperature, w is vertical velocity, z is height, t is time, and S_θ represents the heat source from the canopy. The overbar represents a 5-min-averaging process, and the prime depicts deviations from that average. Using observed profiles of 5-min-averaged winds, temperature, and specific humidity to drive the multilevel canopy model, vertical profiles of S_θ can be predicted. Driving the multilevel canopy model using data from CHATS's entire final month, Fig. A1 presents an evaluation of the model's ability to close the heat budget [i.e., comparing measured vs modeled quantities in Eq. (A1) averaged over 1 h].

Figure A1 shows that the multilevel canopy model provides sufficient realism to investigate the importance of leaf-level processes on turbulence–canopy coupling; this is especially the case since the parameters describing the canopy properties came directly from MEGAN [see Table 2 (Guenther et al. 2006)], are representative of a generic broadleaf forest, and have not been tuned for the CHATS walnut canopy.

REFERENCES

- Albertson, J. D., G. G. Katul, and P. Wiberg, 2001: Relative importance of local and regional controls on coupled water, carbon and energy fluxes. *Adv. Water Resour.*, **24**, 1103–1118, doi:10.1016/S0309-1708(01)00042-2.
- Baldocchi, D. D., and T. P. Meyers, 1988: A spectral and lag-correlation analysis of turbulence in a deciduous forest canopy. *Bound.-Layer Meteor.*, **45**, 31–58, doi:10.1007/BF00120814.
- Beare, R. J., and Coauthors, 2006: An intercomparison of large-eddy simulations of the stable boundary layer. *Bound.-Layer Meteor.*, **118**, 247–272, doi:10.1007/s10546-004-2820-6.
- Beets, C., and B. Koren, 1996: Large-eddy simulation with accurate implicit subgrid-scale diffusion. Centrum voor Wiskunde en Informatica Tech. Rep. NM-R9601, 24 pp.
- Bohrer, G., G. G. Katul, R. L. Walko, and R. Avissar, 2009: Exploring the effects of microscale structural heterogeneity of forest canopies using large-eddy simulations. *Bound.-Layer Meteor.*, **132**, 351–382, doi:10.1007/s10546-009-9404-4.
- Bonan, G. B., 1996: A land surface model (LSM version 1.0) for ecological, hydrological, and atmospheric studies: Technical description and user's guide. NCAR Tech. Rep. NCAR/TN-417+STR, 150 pp.
- , 2008: Forests and climate change: Forcings, feedbacks, and the climate benefits of forests. *Science*, **320**, 1444–1449, doi:10.1126/science.1155121.
- Brunet, Y., J. J. Finnigan, and M. R. Raupach, 1994: A wind tunnel study of air flow in waving wheat: Single-point velocity statistics. *Bound.-Layer Meteor.*, **70**, 95–132, doi:10.1007/BF00712525.
- Brutsaert, W., 1975: On a derivable formula for long-wave radiation from clear skies. *Water Resour. Res.*, **11**, 742–744, doi:10.1029/WR011i005p00742.
- Canadell, J. G., and E. D. Schulze, 2014: Global potential of biospheric carbon management for climate mitigation. *Nat. Commun.*, **5**, 5282, doi:10.1038/ncomms6282.
- Cava, D., and G. G. Katul, 2008: Spectral short-circuiting and wake production within the canopy trunk space of an alpine hardwood forest. *Bound.-Layer Meteor.*, **126**, 415–431, doi:10.1007/s10546-007-9246-x.
- Chen, F., and J. Dudhia, 2001: Coupling an advanced land surface–hydrology model with the Penn State–NCAR MM5 modeling system. Part I: Model implementation and sensitivity. *Mon. Wea. Rev.*, **129**, 569–585, doi:10.1175/1520-0493(2001)129<0569:CAALSH>2.0.CO;2.
- , and Coauthors, 1996: Modeling of land surface evaporation by four schemes and comparison with FIFE observations. *J. Geophys. Res.*, **101**, 7251–7268, doi:10.1029/95JD02165.
- , and Coauthors, 2007: Description and evaluation of the characteristics of the NCAR High-Resolution Land Data Assimilation System. *J. Appl. Meteor. Climatol.*, **46**, 694–713, doi:10.1175/JAM2463.1.
- Collatz, G. J., J. T. Ball, C. Grivet, and J. A. Berry, 1991: Physiological and environmental regulation of stomatal conductance, photosynthesis and transpiration: A model that includes a laminar boundary layer. *Agric. For. Meteor.*, **54**, 107–136, doi:10.1016/0168-1923(91)90002-8.
- , M. Ribas-Carbo, and J. A. Berry, 1992: Coupled photosynthesis–stomatal conductance model for leaves of C₄ plants. *Aust. J. Plant Physiol.*, **19**, 519–538, doi:10.1071/PP9920519.
- Couveaux, F., F. Guichard, J.-L. Redelsperger, C. Kiemle, V. Masson, J.-P. Lafore, and C. Flamant, 2005: Water-vapour variability within a convective boundary-layer assessed by large-eddy simulations and IHOP_2002 observations. *Quart. J. Roy. Meteor. Soc.*, **131**, 2665–2693, doi:10.1256/qj.04.167.
- , V. Masson, and J.-L. Redelsperger, 2007: Negative water vapour skewness and dry tongues in the convective boundary layer: Observations and large-eddy simulation budget analysis. *Bound.-Layer Meteor.*, **123**, 269–294, doi:10.1007/s10546-006-9140-y.
- Davis, K. J., N. Gamage, C. R. Hagelberg, C. Kiemle, D. H. Lenschow, and P. P. Sullivan, 2000: An objective method for deriving atmospheric structure from airborne lidar observations. *J. Atmos. Oceanic Technol.*, **17**, 1455–1468, doi:10.1175/1520-0426(2000)017<1455:AOMFDA>2.0.CO;2.
- Deardorff, J. W., 1972: Numerical investigation of neutral and unstable planetary boundary layers. *J. Atmos. Sci.*, **29**, 91–115, doi:10.1175/1520-0469(1972)029<0091:NIONAU>2.0.CO;2.
- , 1980: Stratocumulus-capped mixed layers derived from a three-dimensional model. *Bound.-Layer Meteor.*, **18**, 495–527, doi:10.1007/BF00119502.
- de Roode, S. R., P. G. Duynkerke, and H. J. J. Jonker, 2004: Large-eddy simulation: How large is large enough? *J. Atmos. Sci.*, **61**, 403–421, doi:10.1175/1520-0469(2004)061<0403:LSHLIL>2.0.CO;2.
- Dupont, S., and Y. Brunet, 2008: Influence of foliar density profile on canopy flow: A large-eddy simulation study. *Agric. For. Meteor.*, **148**, 976–990, doi:10.1016/j.agrformet.2008.01.014.
- , and E. G. Patton, 2012a: Influence of stability and seasonal canopy changes on micrometeorology within and above an orchard canopy: The CHATS experiment. *Agric. For. Meteor.*, **157**, 11–29, doi:10.1016/j.agrformet.2012.01.011.
- , and —, 2012b: Momentum and scalar transport within a vegetation canopy following atmospheric stability and seasonal canopy changes: The CHATS experiment. *Atmos. Chem. Phys.*, **12**, 5913–5935, doi:10.5194/acp-12-5913-2012.
- Dwyer, M. J., E. G. Patton, and R. H. Shaw, 1997: Turbulent kinetic energy budgets from a large-eddy simulation of airflow above

- and within a forest canopy. *Bound.-Layer Meteor.*, **84**, 23–43, doi:[10.1023/A:1000301303543](https://doi.org/10.1023/A:1000301303543).
- Ek, M. B., K. E. Mitchell, Y. Lin, E. Rogers, P. Grunmann, V. Koren, G. Gayno, and J. D. Tarpley, 2003: Implementation of Noah land surface model advances in the National Centers for Environmental Prediction operational mesoscale Eta model. *J. Geophys. Res.*, **108**, 8851, doi:[10.1029/2002JD003296](https://doi.org/10.1029/2002JD003296).
- Falk, M., R. D. Pyles, S. L. Ustin, K. T. Paw U, L. Xu, M. L. Whiting, B. L. Sanden, and P. H. Brown, 2014: Evaluated crop evapotranspiration over a region of irrigated orchards with the improved ACASA-WRF Model. *J. Hydrometeor.*, **15**, 744–758, doi:[10.1175/JHM-D-12-0183.1](https://doi.org/10.1175/JHM-D-12-0183.1).
- FAO, 2010: Global Forest Resources Assessment 2010: Main report. FAO Tech. Rep. 163, 378 pp. [Available online at <http://www.fao.org/docrep/013/i1757e/i1757e.pdf>.]
- Finnigan, J. J., 1985: Turbulent transport in flexible plant canopies. *The Forest–Atmosphere Interaction*, B. A. Hutchison and B. B. Hicks, Eds., Springer Netherlands, 443–480.
- , and R. H. Shaw, 2008: Double-averaging methodology and its application to turbulent flow in and above vegetation canopies. *Acta Geophys.*, **56**, 534–561, doi:[10.2478/s11600-008-0034-x](https://doi.org/10.2478/s11600-008-0034-x).
- , R. Clement, Y. Malhi, R. Leuning, and H. A. Cleugh, 2003: A re-evaluation of long-term flux measurement techniques. Part I: Averaging and coordinate rotation. *Bound.-Layer Meteor.*, **107**, 1–48, doi:[10.1023/A:1021554900225](https://doi.org/10.1023/A:1021554900225).
- , R. H. Shaw, and E. G. Patton, 2009: Turbulence structure above a vegetation canopy. *J. Fluid Mech.*, **637**, 387–424, doi:[10.1017/S0022112009990589](https://doi.org/10.1017/S0022112009990589).
- Fuentes, J. D., and Coauthors, 2000: Biogenic hydrocarbons in the atmospheric boundary layer: A review. *Bull. Amer. Meteor. Soc.*, **81**, 1537–1575, doi:[10.1175/1520-0477\(2000\)081<1537: BHITAB>2.3.CO;2](https://doi.org/10.1175/1520-0477(2000)081<1537: BHITAB>2.3.CO;2).
- Gao, W., R. H. Shaw, and K. T. Paw U, 1992: Conditional analysis of temperature and humidity microfronts and ejection/sweep motions within and above a deciduous forest. *Bound.-Layer Meteor.*, **59**, 35–57, doi:[10.1007/BF00120685](https://doi.org/10.1007/BF00120685).
- Goudriaan, J., and H. H. van Laar, 1994: *Modelling Potential Crop Growth Processes*. Kluwer Academic Publishers, 256 pp.
- Guenther, A., P. R. Zimmerman, P. C. Harley, R. K. Monson, and R. Fall, 1993: Isoprene and monoterpene emission rate variability: Model evaluations and sensitivity analyses. *J. Geophys. Res.*, **98**, 12 609–12 617, doi:[10.1029/93JD00527](https://doi.org/10.1029/93JD00527).
- , and Coauthors, 1995: A global model of natural volatile organic compound emissions. *J. Geophys. Res.*, **100**, 8873–8892, doi:[10.1029/94JD02950](https://doi.org/10.1029/94JD02950).
- , T. Karl, P. Harley, C. Wiedinmyer, P. I. Palmer, and C. Geron, 2006: Estimates of global terrestrial isoprene emissions using MEGAN (Model of Emissions of Gases and Aerosols from Nature). *Atmos. Chem. Phys.*, **6**, 3181–3210, doi:[10.5194/acp-6-3181-2006](https://doi.org/10.5194/acp-6-3181-2006).
- Harman, I. N., and J. J. Finnigan, 2007: A simple unified theory for flow in the canopy and roughness sublayer. *Bound.-Layer Meteor.*, **123**, 339–363, doi:[10.1007/s10546-006-9145-6](https://doi.org/10.1007/s10546-006-9145-6).
- , and —, 2008: Scalar concentration profiles in the canopy and roughness sublayer. *Bound.-Layer Meteor.*, **129**, 323–351, doi:[10.1007/s10546-008-9328-4](https://doi.org/10.1007/s10546-008-9328-4).
- Huang, J., G. Katul, and J. Albertson, 2013: The role of coherent turbulent structures in explaining scalar dissimilarity within the canopy sublayer. *Environ. Fluid Mech.*, **13**, 571–599, doi:[10.1007/s10652-013-9280-9](https://doi.org/10.1007/s10652-013-9280-9).
- Hunt, J. C. R., and J. M. R. Graham, 1978: Free-stream turbulence near plane boundaries. *J. Fluid Mech.*, **84**, 209–235, doi:[10.1017/S0022112078000130](https://doi.org/10.1017/S0022112078000130).
- Hutchins, N., and I. Marusic, 2007: Evidence of very long meandering features in the logarithmic region of turbulent boundary layers. *J. Fluid Mech.*, **579**, 1–28, doi:[10.1017/S0022112006003946](https://doi.org/10.1017/S0022112006003946).
- Kaimal, J. C., and J. J. Finnigan, 1994: *Atmospheric Boundary Layer Flows: Their Structure and Measurement*. Oxford University Press, 289 pp.
- , J. C. Wyngaard, Y. Izumi, and O. R. Coté, 1972: Spectral characteristics of surface layer turbulence. *Quart. J. Roy. Meteor. Soc.*, **98**, 563–589, doi:[10.1002/qj.49709841707](https://doi.org/10.1002/qj.49709841707).
- Katul, G. G., C.-I. Hsieh, G. Kuhn, and D. Ellsworth, 1997: Turbulent eddy motion at the forest–atmosphere interface. *J. Geophys. Res.*, **102**, 13 409–13 421, doi:[10.1029/97JD00777](https://doi.org/10.1029/97JD00777).
- , C. D. Geron, C.-I. Hsieh, B. Vidakovic, and A. B. Guenther, 1998a: Active turbulence and scalar transport near the forest–atmosphere interface. *J. Appl. Meteor.*, **37**, 1533–1546, doi:[10.1175/1520-0450\(1998\)037<1533:ATASN>2.0.CO;2](https://doi.org/10.1175/1520-0450(1998)037<1533:ATASN>2.0.CO;2).
- , J. Schieldge, C.-I. Hsieh, and B. Vidakovic, 1998b: Skin temperature perturbations induced by surface layer turbulence above a grass surface. *Water Resour. Res.*, **34**, 1265–1274, doi:[10.1029/98WR00293](https://doi.org/10.1029/98WR00293).
- Khanna, S., and J. G. Brasseur, 1998: Three-dimensional buoyancy- and shear-induced local structure of the atmospheric boundary layer. *J. Atmos. Sci.*, **55**, 710–743, doi:[10.1175/1520-0469\(1998\)055<0710:TDBASI>2.0.CO;2](https://doi.org/10.1175/1520-0469(1998)055<0710:TDBASI>2.0.CO;2).
- Lamaud, E., and M. Irvine, 2006: Temperature–humidity dissimilarity and heat-to-water-vapour transport efficiency above and within a pine forest canopy: The role of the Bowen ratio. *Bound.-Layer Meteor.*, **120**, 87–109, doi:[10.1007/s10546-005-9032-6](https://doi.org/10.1007/s10546-005-9032-6).
- Leclerc, M. Y., K. C. Beissner, R. H. Shaw, G. Hartog, and H. H. Neumann, 1991: The influence of buoyancy on third-order turbulent velocity statistics within a deciduous forest. *Bound.-Layer Meteor.*, **55**, 109–123, doi:[10.1007/BF00119329](https://doi.org/10.1007/BF00119329).
- Lenschow, D. H., J. Mann, and L. Kristensen, 1994: How long is long enough when measuring fluxes and other turbulent statistics. *J. Atmos. Oceanic Technol.*, **11**, 661–673, doi:[10.1175/1520-0426\(1994\)011<0661:HLILEW>2.0.CO;2](https://doi.org/10.1175/1520-0426(1994)011<0661:HLILEW>2.0.CO;2).
- , M. Lothon, S. D. Mayor, P. P. Sullivan, and G. Canut, 2012: A comparison of higher-order vertical velocity moments in the convective boundary layer from lidar with in situ measurements and large-eddy simulation. *Bound.-Layer Meteor.*, **143**, 107–123, doi:[10.1007/s10546-011-9615-3](https://doi.org/10.1007/s10546-011-9615-3).
- Le Quéré, C., and Coauthors, 2014: Global carbon budget 2013. *Earth Syst. Sci. Data*, **6**, 235–263, doi:[10.5194/essd-6-235-2014](https://doi.org/10.5194/essd-6-235-2014).
- Leuning, R., 1990: Modeling stomatal behavior and photosynthesis of *Eucalyptus grandis*. *Aust. J. Plant Physiol.*, **17**, 159–175, doi:[10.1071/PP9900159](https://doi.org/10.1071/PP9900159).
- , 1997: Scaling to a common temperature improves the correlation relation between the photosynthesis parameters J_{max} and V_{cmax} . *J. Exp. Bot.*, **48**, 345–347, doi:[10.1093/jxb/48.2.345](https://doi.org/10.1093/jxb/48.2.345).
- , F. M. Kelliher, D. G. G. de Pury, and E.-D. Schulze, 1995: Leaf nitrogen, photosynthesis, conductance and transpiration: Scaling from leaves to canopies. *Plant Cell Environ.*, **18**, 1183–1200, doi:[10.1111/j.1365-3040.1995.tb00628.x](https://doi.org/10.1111/j.1365-3040.1995.tb00628.x).
- Li, D., and E. Bou-Zeid, 2011: Coherent structures and the dissimilarity of turbulent atmospheric surface layer. *Bound.-Layer Meteor.*, **140**, 243–262, doi:[10.1007/s10546-011-9613-5](https://doi.org/10.1007/s10546-011-9613-5).
- Mahrt, L., 1991: Boundary-layer moisture regimes. *Quart. J. Roy. Meteor. Soc.*, **117**, 151–176, doi:[10.1002/qj.49711749708](https://doi.org/10.1002/qj.49711749708).
- Moene, A. F., B. I. Michels, and A. A. M. Holtslag, 2006: Scaling variances of scalars in a convective boundary layer under different entrainment regimes. *Bound.-Layer Meteor.*, **120**, 257–274, doi:[10.1007/s10546-006-9053-9](https://doi.org/10.1007/s10546-006-9053-9).

- Moeng, C.-H., 1984: A large-eddy-simulation model for the study of planetary boundary-layer turbulence. *J. Atmos. Sci.*, **41**, 2052–2062, doi:[10.1175/1520-0469\(1984\)041<2052:ALESMF>2.0.CO;2](https://doi.org/10.1175/1520-0469(1984)041<2052:ALESMF>2.0.CO;2).
- , and J. C. Wyngaard, 1988: Spectral analysis of large-eddy simulations of the convective boundary layer. *J. Atmos. Sci.*, **45**, 3573–3587, doi:[10.1175/1520-0469\(1988\)045<3573:SAOLES>2.0.CO;2](https://doi.org/10.1175/1520-0469(1988)045<3573:SAOLES>2.0.CO;2).
- , and R. Rotunno, 1990: Vertical velocity skewness in the buoyancy-driven boundary layer. *J. Atmos. Sci.*, **47**, 1149–1162, doi:[10.1175/1520-0469\(1990\)047<1149:VVSTIB>2.0.CO;2](https://doi.org/10.1175/1520-0469(1990)047<1149:VVSTIB>2.0.CO;2).
- , and P. P. Sullivan, 1994: A comparison of shear- and buoyancy-driven planetary boundary layer flows. *J. Atmos. Sci.*, **51**, 999–1022, doi:[10.1175/1520-0469\(1994\)051<0999:ACOSAB>2.0.CO;2](https://doi.org/10.1175/1520-0469(1994)051<0999:ACOSAB>2.0.CO;2).
- Monteith, J. L., 1973: *Principles of Environmental Physics*. Edward Arnold Limited, 241 pp.
- , and M. H. Unsworth, 2008: *Principles of Environmental Physics*. 3rd ed. Elsevier, 418 pp.
- Nikolov, N. T., W. J. Massman, and A. W. Schoettle, 1995: Coupling biochemical and biophysical processes at the leaf level: An equilibrium photosynthesis model for leaves of C_3 plants. *Ecol. Modell.*, **80**, 205–235, doi:[10.1016/0304-3800\(94\)00072-P](https://doi.org/10.1016/0304-3800(94)00072-P).
- Niyogi, D., K. Alapaty, S. Raman, and F. Chen, 2009: Development and evaluation of a coupled photosynthesis-based gas exchange evapotranspiration model (GEM) for mesoscale weather forecasting applications. *J. Appl. Meteor. Climatol.*, **48**, 349–368, doi:[10.1175/2008JAMC1662.1](https://doi.org/10.1175/2008JAMC1662.1).
- Orszag, S. A., 1969: Numerical methods for the simulation of turbulence. *Phys. Fluids*, **12**, II-250, doi:[10.1063/1.1692445](https://doi.org/10.1063/1.1692445).
- Pan, H.-L., and L. Mahrt, 1987: Interaction between soil hydrology and boundary layer development. *Bound.-Layer Meteor.*, **38**, 185–202, doi:[10.1007/BF00121563](https://doi.org/10.1007/BF00121563).
- Pan, Y., M. Chamecki, and S. A. Isard, 2014a: Large-eddy simulation of turbulence and particle dispersion inside the canopy roughness sublayer. *J. Fluid Mech.*, **753**, 499–534, doi:[10.1017/jfm.2014.379](https://doi.org/10.1017/jfm.2014.379).
- , E. Follett, M. Chamecki, and H. Nepf, 2014b: Strong and weak, unsteady reconfiguration and its impact on turbulence structure within plant canopies. *Phys. Fluids*, **26**, 105102, doi:[10.1063/1.4898395](https://doi.org/10.1063/1.4898395).
- Patton, E. G., 1997: Large-eddy simulation of turbulent flow above and within a plant canopy. Ph.D. thesis, University of California, Davis, 145 pp.
- , K. J. Davis, M. C. Barth, and P. P. Sullivan, 2001: Decaying scalars emitted by a forest canopy: A numerical study. *Bound.-Layer Meteor.*, **100**, 91–129, doi:[10.1023/A:1019223515444](https://doi.org/10.1023/A:1019223515444).
- , P. P. Sullivan, and K. J. Davis, 2003: The influence of a forest canopy on top-down and bottom-up diffusion in the planetary boundary layer. *Quart. J. Roy. Meteor. Soc.*, **129**, 1415–1434, doi:[10.1256/qj.01.175](https://doi.org/10.1256/qj.01.175).
- , —, and C.-H. Moeng, 2005: The influence of idealized heterogeneity on wet and dry planetary boundary layers coupled to the land surface. *J. Atmos. Sci.*, **62**, 2078–2097, doi:[10.1175/JAS3465.1](https://doi.org/10.1175/JAS3465.1).
- , and Coauthors, 2011: The canopy horizontal array turbulence study. *Bull. Amer. Meteor. Soc.*, **92**, 593–611, doi:[10.1175/2010BAMS2614.1](https://doi.org/10.1175/2010BAMS2614.1).
- Raupach, M. R., and A. S. Thom, 1981: Turbulence in and above plant canopies. *Annu. Rev. Fluid Mech.*, **13**, 97–129, doi:[10.1146/annurev.fl.13.010181.000525](https://doi.org/10.1146/annurev.fl.13.010181.000525).
- , and R. H. Shaw, 1982: Averaging procedures for flow within vegetation canopies. *Bound.-Layer Meteor.*, **22**, 79–90, doi:[10.1007/BF00128057](https://doi.org/10.1007/BF00128057).
- , J. J. Finnigan, and Y. Brunet, 1996: Coherent eddies and turbulence in vegetation canopies: The mixing-layer analogy. *Bound.-Layer Meteor.*, **78**, 351–382, doi:[10.1007/BF00120941](https://doi.org/10.1007/BF00120941).
- Schmidt, H., and U. Schumann, 1989: Coherent structure of the convective boundary layer derived from large-eddy simulation. *J. Fluid Mech.*, **200**, 511–562, doi:[10.1017/S0022112089000753](https://doi.org/10.1017/S0022112089000753).
- Shaw, R. H., 1977: Secondary wind speed maxima inside plant canopies. *J. Appl. Meteor.*, **16**, 514–521, doi:[10.1175/1520-0450\(1977\)016<0514:SWSMIP>2.0.CO;2](https://doi.org/10.1175/1520-0450(1977)016<0514:SWSMIP>2.0.CO;2).
- , and U. Schumann, 1992: Large-eddy simulation of turbulent flow above and within a forest. *Bound.-Layer Meteor.*, **61**, 47–64, doi:[10.1007/BF02033994](https://doi.org/10.1007/BF02033994).
- , and E. G. Patton, 2003: Canopy element influences on resolved- and subgrid-scale energy within a large-eddy simulation. *Agric. For. Meteor.*, **115**, 5–17, doi:[10.1016/S0168-1923\(02\)00165-X](https://doi.org/10.1016/S0168-1923(02)00165-X).
- , G. Hartog, and H. H. Neumann, 1988: Influence of foliar density and thermal stability on profiles of Reynolds stress and turbulence intensity in a deciduous forest. *Bound.-Layer Meteor.*, **45**, 391–409, doi:[10.1007/BF00124010](https://doi.org/10.1007/BF00124010).
- , K. T. Paw U, X. J. Zhang, W. Gao, G. Hartog, and H. H. Neumann, 1990: Retrieval of turbulent pressure fluctuations at the ground surface beneath a forest. *Bound.-Layer Meteor.*, **50**, 319–338, doi:[10.1007/BF00120528](https://doi.org/10.1007/BF00120528).
- , Y. Brunet, J. J. Finnigan, and M. R. Raupach, 1995: A wind tunnel study of air flow in waving wheat: Two-point velocity statistics. *Bound.-Layer Meteor.*, **76**, 349–376, doi:[10.1007/BF00709238](https://doi.org/10.1007/BF00709238).
- Spalart, P. R., R. D. Moser, and M. M. Rogers, 1991: Spectral methods for the Navier–Stokes equations with one infinite and two periodic directions. *J. Comput. Phys.*, **96**, 297–324, doi:[10.1016/0021-9991\(91\)90238-G](https://doi.org/10.1016/0021-9991(91)90238-G).
- Stull, R. B., 1988: *An Introduction to Boundary Layer Meteorology*. Kluwer Academic Publishers, 666 pp.
- Su, H.-B., R. H. Shaw, K. T. Paw U, C.-H. Moeng, and P. P. Sullivan, 1998: Turbulent statistics of neutrally stratified flow within and above a sparse forest from large-eddy simulation and field observation. *Bound.-Layer Meteor.*, **88**, 363–397, doi:[10.1023/A:1001108411184](https://doi.org/10.1023/A:1001108411184).
- , —, and —, 2000: Two-point correlation analysis of neutrally stratified flow within and above a forest from large-eddy simulation. *Bound.-Layer Meteor.*, **94**, 423–460, doi:[10.1023/A:1002430213742](https://doi.org/10.1023/A:1002430213742).
- , H. P. Schmid, C. S. B. Grimmond, C. S. Vogel, and A. J. Oliphant, 2004: Spectral characteristics and long-term eddy-covariance measurements over two mixed hardwood forests in non-flat terrain. *Bound.-Layer Meteor.*, **110**, 213–253, doi:[10.1023/A:1026099523505](https://doi.org/10.1023/A:1026099523505).
- Sullivan, P. P., and E. G. Patton, 2011: The effect of mesh resolution on convective boundary layer statistics and structures generated by large-eddy simulation. *J. Atmos. Sci.*, **68**, 2395–2415, doi:[10.1175/JAS-D-10-05010.1](https://doi.org/10.1175/JAS-D-10-05010.1).
- , J. C. McWilliams, and C.-H. Moeng, 1994: A subgrid-scale model for large-eddy simulation of planetary boundary-layer flows. *Bound.-Layer Meteor.*, **71**, 247–276, doi:[10.1007/BF00713741](https://doi.org/10.1007/BF00713741).
- , —, and —, 1996: A grid nesting method for large-eddy simulation of planetary boundary-layer flows. *Bound.-Layer Meteor.*, **80**, 167–202, doi:[10.1007/BF00119016](https://doi.org/10.1007/BF00119016).
- , C.-H. Moeng, B. Stevens, D. H. Lenschow, and S. D. Mayor, 1998: Structure of the entrainment zone capping the convective

- atmospheric boundary layer. *J. Atmos. Sci.*, **55**, 3042–3064, doi:[10.1175/1520-0469\(1998\)055<3042:SOTEZC>2.0.CO;2](https://doi.org/10.1175/1520-0469(1998)055<3042:SOTEZC>2.0.CO;2).
- Thom, A. S., 1968: The exchange of momentum, mass, and heat between an artificial leaf and the airflow in a wind tunnel. *Quart. J. Roy. Meteor. Soc.*, **94**, 44–55, doi:[10.1002/qj.49709439906](https://doi.org/10.1002/qj.49709439906).
- Thomas, C., and T. Foken, 2007: Organised motion in a tall spruce canopy: Temporal scales, structure spacing and terrain effects. *Bound.-Layer Meteor.*, **122**, 123–147, doi:[10.1007/s10546-006-9087-z](https://doi.org/10.1007/s10546-006-9087-z).
- van de Boer, A., A. F. Moene, A. Graf, D. Schüttemeyer, and C. Simmer, 2014: Detection of entrainment influences on surface-layer measurements and extension of Monin–Obukhov similarity theory. *Bound.-Layer Meteor.*, **152**, 19–44, doi:[10.1007/s10546-014-9920-8](https://doi.org/10.1007/s10546-014-9920-8).
- Wallace, J. M., H. Eckelmann, and R. S. Brodkey, 1972: The wall region in turbulent shear flow. *J. Fluid Mech.*, **54**, 39–48, doi:[10.1017/S0022112072000515](https://doi.org/10.1017/S0022112072000515).
- Welgepolage, K., A. S. M. Gieske, C. van der Tol, J. Timmermans, and Z. Su, 2012: Effect of sub-layer corrections on the roughness parameterization of a Douglas fir forest. *Agric. For. Meteor.*, **162–163**, 115–126, doi:[10.1016/j.agrformet.2012.04.017](https://doi.org/10.1016/j.agrformet.2012.04.017).
- Wesson, K. H., G. G. Katul, and M. Siqueira, 2003: Quantifying organization of atmospheric turbulent eddy motion using nonlinear time series analysis. *Bound.-Layer Meteor.*, **106**, 507–525, doi:[10.1023/A:1021226722588](https://doi.org/10.1023/A:1021226722588).
- Willmarth, W. W., and S. S. Lu, 1972: Structure of the Reynolds stress near the wall. *J. Fluid Mech.*, **55**, 65–92, doi:[10.1017/S002211207200165X](https://doi.org/10.1017/S002211207200165X).
- Wyngaard, J. C., 2010: *Turbulence in the Atmosphere*. Cambridge University Press, 393 pp.
- , O. R. Coté, and Y. Izumi, 1971: Local free convection, similarity, and the budgets of shear stress and heat flux. *J. Atmos. Sci.*, **28**, 1171–1182, doi:[10.1175/1520-0469\(1971\)028<1171:LFCSAT>2.0.CO;2](https://doi.org/10.1175/1520-0469(1971)028<1171:LFCSAT>2.0.CO;2).